NOAA ATLAS No. 13

Atlas of the Tropical Pacific Ocean Annual Cycle

Camp Springs, Md.
May 1994

U.S. DEPARTMENT OF COMMERCE
National Oceanic and Atmospheric Administration
National Weather Service

NOAA ATLAS No. 13

Atlas of the Tropical Pacific Ocean Annual Cycle

Thomas M. Smith, Muthuvel Chelliah
Climate Analysis Center
National Meteorological Center
National Weather Service

Camp Springs, MD.
May 1994

U.S. DEPARTMENT OF COMMERCE
Ronald H. Brown, Secretary
National Oceanic and Atmospheric Administration
Dr. D. James Baker, Under Secretary
National Weather Service
Dr. Elbert W. Friday, Jr., Assistant Administrator

TABLE OF CONTENTS

Atlas of the Tropical Pacific Ocean Annual Cycle

Abstract

Data for this tropical Pacific ocean atlas comes from monthly gridded analyses of temperature and current data over a ten year (1983-1992) period generated by an ocean-data assimilation system at the National Meteorological Center, Washington D.C. This atlas shows maps of the long-term mean, monthly standard deviation, mean annual cycle (harmonic dial) and the amount of variance explained by the annual cycle for surface and subsurface quantities of the tropical Pacific Ocean. The main focus of this atlas is subsurface variations, but the surface wind-stress curl and sea-surface temperature are also included for completeness. The main variables considered here are subsurface temperature, currents, and the depth of the 20°C isotherm. A few trajectories of water parcels along the depth of the 20°C isotherm during the course of the annual cycle are also shown. Data are shown on level surfaces at selected depths, depth integrated, and on meridional and zonal cross sections.

Introduction

The annual cycle of the tropical Pacific Ocean needs to be understood so that interannual variations can be quantified and sometimes interpreted as amplification, weakening, breakdown, or phase shifts of the normal annual cycle. Climatological oceanic conditions in the tropical Pacific have been studied in the past using both observations and models (e.g., Wyrtki *et al.* 1981a, Bryden and Brady 1985, Philander *et al.* 1987). Surface wind-stress climatologies have also been compiled earlier (e.g., Hellerman and Rosenstein 1983, Harrison 1989) and were used by ocean models to simulate the ocean's upper layer. To date, most oceanic climatologies include only surface variables (e.g., Horel 1982, Halpert and Ropelewski 1989, Shea *et al.* 1992). Because of large surface data sets, such as COADS, the SST climatology is fairly well known. Subsurface observations are more sparse. However, Levitus (1982) has generated a comprehensive three-dimensional atlas of oceanic fields, but he had to combine irregularly distributed data, both spatially and temporally, over approximately 80 years.

In this study we compute a Pacific Ocean climatology using data generated by an ocean-data assimilation system (ODAS) at the Coupled Model Project/NMC. This atlas supplements studies of the annual cycle and interannual variability in preparation by Smith and Chelliah, which give more in depth discussion of both the annual cycle and interannual variations. The oceanic analysis using the ODAS is analogous to atmospheric analyses that have been done at NMC for many years, and are the basis for many large scale studies of the atmosphere (e.g., Kousky and Leetmaa 1989). In fact, these ocean analyses are routinely used by the Climate Analysis Center at NMC to monitor the current status of the El Niño Southern Oscillation

(ENSO) on an operational basis (Climate Diagnostics Bulletin, ENSO Advisory). Observations are assimilated into an ocean general circulation model (GCM) to estimate conditions over a large region, using an incomplete network of observations. The ODAS uses the model equations to extrapolate the available observations throughout the basin (Ji *et al.* 1994a) to a regular latitude-longitude grid.

Data, Analysis, and Validation

Ocean reanalysis at NMC uses an ODAS that has evolved continuously since 1985 (Leetmaa and Ji 1989). The ODAS consists of essentially the same ocean GCM as described by Leetmaa and Ji (1989) but uses improved assimilation methods (Derber and Rosati 1989). The ocean GCM for the tropical Pacific was originally developed at the Geophysical Fluid Dynamics Laboratory (Bryan 1969, Cox 1984, Philander *et al.* 1987). In the version used for this study the ocean GCM used realistic bottom topography. It has an east-west domain from 120°E to 70°W with a constant resolution of 1.5°, and a north-south domain from 45°S to 55°N with variable resolution from 1/3° within 10° of the equator increasing gradually to 1° outside of 20° latitude. Within 10° of the northern and southern boundaries the model fields are relaxed to the climatological estimates of Levitus (1982), with time scales decreasing from 150 days at 10° from the boundaries to 5 days at the boundaries. There are 28 vertical levels with a resolution of 10 m in the upper 100 m, gradually becoming more coarse with depth. The greatest possible depth in the model is 4151 m.

The ODAS assimilates all available surface and subsurface temperature data from

expendable bathythermographs (XBTs) and moored buoys. The blended SST (Reynolds and Marsico 1993), is used before April 1988, and a higher resolution SST (Reynolds and Smith 1993) is used afterwards. Both SST data sets use ship, buoy, and satellite measurements. Because of satellite data, SST is densely sampled over the entire area. The number of XBTs per month between 20°N and 20°S is shown by Fig. 1a. Observations generally increase from 1983 to about the middle of 1987, when they decrease a little bit, and increase again. The XBTs are carefully checked to remove erroneous values. They extend to an average depth of about 450 m and are used to a maximum depth of 720 m in the tropical Pacific. While XBTs generally follow ship tracks across the oceans, the sample plots of Levitus and Gelfeld (1992) show that the coverage of the tropical Pacific is generally better in the 1980s than in earlier years. The TOGA-TAO array of moored buoys gives subsurface temperatures near the equator across most of the Pacific beginning in the mid 1980s (Hayes *et al.* 1991). A sample distribution of available subsurface data is shown in Fig. 1b for October 1991. Dots and crosses represent the XBT observations and TOGA-TAO moorings respectively. The October 1991 XBT distribution, which is typical of the longer period, cover most of the tropical Pacific but is less dense in the eastern tropical Pacific, where the TOGA-TAO array is most important. The lack of TOGA-TAO moorings before about 1985 suggests that during the early years the analyzed data should be less reliable near the equator.

Assimilation requires the use of horizontal e-folding correlation scales, which define the influence of an observation upon its surroundings. The assimilation is done separately at each horizontal level with no vertical coupling, although there is some vertical smoothing between

levels. Correlation e-folding scales are four degrees at the equator, decreasing away from the equator proportional to the cosine of the latitude. All data from a two week period centered on the integration time are used in the assimilation. Use of this time window effectively increases the amount of data at each time step while still resolving variations with frequencies greater than a month.

To get the surface momentum flux for the ODAS, wind-stress anomalies from an atmospheric GCM forced by observed SST, are added to the climatological surface wind stress. The atmospheric GCM is a low-resolution (T40, horizontal resolution of 320 km) version of th NMC's e operational medium-range spectral forecast model, using smoothed topography. Among the many changes (Ji *et al.* 1994b) that were made to the forecast model to best fit in for climate studies, the adjustment made to allow for the development of more organized tropical convection is a significant one. Two separate atmospheric simulations, using slightly different initial conditions, were done from January 1982 to December 1992. The two atmospheric simulations were then averaged. Anomalies of the model's monthly average surface wind stress are computed with respect to its ten-year climatology, to preserve only those anomalies induced by the SST variations. These anomalies are then added onto the wind stress climatology constructed from Harrison (1989) between 20°S and 20°N, Hellerman and Rosenstein (1983) poleward of 30° latitude, and linear interpolation between the two climatologies between 20° and 30° latitude. It should be noted that compared to Florida State University surface stress and wind stress computed from the TOGA-TAO mooring observed winds, the stress used by ODAS has smaller interannual anomalies (Busalacchi, personal communication). However, the slightly weaker

anomalies do not significantly affect the wind stress climatology. Assimilation of temperature observations further reduces the effects of errors in the wind stress.

The present version of the ODAS has no net fresh water flux into the ocean. To keep the salinity from drifting excessively it is reset once a year to the annual climatological values of Levitus (1982). The net heat flux into the ocean model is from the climatology of Oberhuber (1989), but assimilation dominates adjustments of surface temperatures. The abundance of SST observations throughout the period prevents possible inaccuracies in the heat flux from affecting the ODAS temperature analysis.

Detailed validation of the ocean analysis is discussed by Ji *et al.* (1994a). Possible errors in the surface wind stress, noted above, have little effect on the SST because of the large amount of SST observations assimilated into ODAS. Hence, the SST annual cycle described here is not significantly different from the climatology of Shea *et al.* (1992). Ji *et al.* (1994a) compare the dynamic heights computed from the ODAS reanalysis with sea-level observations from island stations, which are not assimilated. Note that dynamic height and sea level both represent the depth-integrated density of the ocean, which varies with ocean heat storage. They find that interannual variations of the dynamic height calculated from reanalysis data follow the sea level observations reasonably well, with typical errors of a few centimeters throughout the tropical Pacific. Note that the range of interannual sea-level variability is about ten times larger than the typical errors.

The mean annual cycle is shown here using the well known harmonic dials (e.g., Halpert and Ropelewski 1989). We first time filter the monthly data using a five-point binomial filter, which strongly reduces variations more frequent than the semiannual cycle. For each filtered field, we compute the ten-year mean and monthly standard deviation, and Fourier series harmonics in time. Harmonics are obtained from all 120 months, but using an assigned period of *12 calendar months*. Thus the first harmonic gives the annual cycle. The total variance less the variance of the sum of the first two harmonics is essentially the low-frequency variance. To describe the annual cycle of various quantities, we show the mean, monthly standard deviation, the percentage of variance explained by the annual cycle, and the annual cycle harmonic dial. The harmonic dial is a vector with a length proportional to the amplitude of the annual cycle and a direction that shows the phase of the annual cycle (vectors < 0.1 maximum are not shown).

Discussion

The purpose of the following discussion is not to present a detailed description of all the figures shown in this atlas, but rather only to highlight the major features of the annual cycle.

1. The Air-Sea Interface

We show here the surface wind-stress curl (Fig. 2) and SST (Figs. 3-5) for the sake of completeness so that they can be viewed in context with the subsurface features, which is the main focus of this atlas, shown in the succeeding sections. Standard deviation of the curl is large near the Inter-Tropical Convergence Zone (ITCZ) in the North Pacific. In the southwestern Pacific there is another high variance region south of the South Pacific Convergence Zone (SPCZ). The annual cycles of the ITCZ and the SPCZ are discussed by Meehl (1987). Seasonal

movements of the ITCZ result in a strong annual cycle of the curl's variance along 3°- 5°N in the eastern Pacific, where the curl is largest in boreal winter. In the eastern Pacific the annual cycle of the curl is also important along the South American coast. In the western Pacific the curl is again largest in the boreal winter near the equator, and in the boreal summer near 20°S eastward to 140°W. The western Pacific annual cycle of the curl is related to monsoonal variations.

The ten-year mean of SST shows the well-known cold tongue in the eastern-equatorial Pacific, extending west to about the date line, similar to other SST analyses (e.g., Horel 1982, Shea *et al.* 1992). Standard deviation of SST is lowest associated with the warmest mean temperatures. In the tropics standard deviation is highest in the eastern-equatorial Pacific and along the South American coast south of the equator. The annual cycle is most important at the equator just off South America, where the cycle of the southeast trades is largest. Eastern-equatorial Pacific SST is warmest in March near the coast, associated with the spring surge of eastward currents (Lukas 1986). A few degrees further west SST is warmest in April.

2. Temperature Cross Sections

Depth-longitude cross sections are shown over the upper 300 m at 10°N, the equator, and 10°S (Figs. 6-8, 12-15). Depth-latitude sections are shown at 165°E, 160°W, and 110°W (Figs. 9-11). The annual mean depth of the 20°C isotherm is also shown on the cross sections, and appears at the center of the annual mean thermocline in these sections. Largest standard deviation values are below the surface, showing the importance of thermocline-depth variations.

At 10°N most surface variance is accounted for by the annual cycle. In the subsurface, the amplitude of the annual cycle is much stronger than at the surface although it accounts for less annual-cycle variance. At the equator the annual cycle at the surface is out of phase with the subsurface annual cycle, and suggests westward surface propagation and eastward subsurface propagation. On the sections most subsurface variance is interannual, so subsurface variations associated with the Southern Oscillation can be expected to be much larger than those associated with the annual cycle. At 10°S there is relatively little subsurface variation, compared to the equator and 10°N. The north-south cross sections show the ocean's troughs and ridges, which are directly related to the zonal ocean currents in the tropical Pacific (Wyrtki 1974).

3. Depths of the 20°C Isotherm

The depth of the 20°C isotherm (Figs. 16-20) is at the center of the main thermocline in the tropical Pacific, which is the depth at which temperature variations are largest. Thus, it is a good indicator of the depth of the upper warm layer in the tropical Pacific ocean. We do not show 20°C isotherm-depth data in regions in which the 20°C isotherm intersects the surface more than 10% of the months, or more than two months in a row. Where the isotherm infrequently comes to the surface linear interpolation in time is used to fill in the missing months. This filling is used for a few months in the eastern equatorial Pacific, where the 20°C isotherm surfaced in 1988. The mean depth shows deep warm layers in both hemispheres in the western tropical Pacific. Of the two warm pools, the South Pacific warm region is larger, deeper, and closer to the equator. The smaller north Pacific warm pool is separated from the equator by the NECC trough, shown by shallower depths along 5°N-10°N. The troughs and ridges along meridional

sections in the tropical Pacific are indicated by depth gradients. North of 7°N-10°N the NEC flows westward, and south of there the NECC flows eastward, while the SEC flows westward between about 10°S and 5°N.

The spatial pattern and the annual cycle of the depth of the 20°C isotherm are in agreement with the limited measurements by Kessler and Taft (1987), and with dynamic height calculations of Taft and Kessler (1991). As in our study, they found the greatest amplitude of the annual cycle near the latitude of the ITCZ. Using a numerical model forced by climatological wind stress, Philander *et al.* (1987) simulated tropical Pacific Ocean heat-storage variations similar to the heat storage variations implied by the of depth of the 20°C isotherm in this study.

4. Subsurface Horizontal Temperature Variations

Besides the depths of the 20°C isotherm, other indicators of upper ocean heat-storage variation include the average temperature over the upper 200 m of the ocean (Fig. 21), and the temperature on level surfaces at 100 m and 200 m (Figs. 22-23). In the tropics, these indicate annual-cycle variations similar to those shown by the depth of the 20°C isotherm. Among these level surfaces the variance near the equator is usually highest at 100 m, which is near the mean thermocline depth in most of the tropical Pacific. In the western Pacific where the thermocline is deeper, there is more variance at 200 m.

5. Ocean Currents

Major zonal currents are well known (e.g., see Philander *et al.* 1987). The most important

currents are: a) the North Equatorial Counter Current (NECC) which flows eastward between about 5°N and 10°N, b) the Equatorial Undercurrent (EUC), which flows eastward below the surface within a few degrees of the equator, c) the South Equatorial Current (SEC) and, d) the North Equatorial Current (NEC), which both flow westward. The SEC extends from about 10°S to 5°N, and becomes shallow across the equator. The NEC is approximately between 10°N to 20°N. To show the current variations we use depth cross sections and zonal averaging of meridional velocities. It should be noted that, at present, the ODAS has been tuned for ocean temperatures, and hence the ocean currents are less reliable.

Horizontal velocity, vertically averaged from the surface to 200 m (Fig. 24) shows a strong eastward flowing EUC, which flows down the equatorial pressure gradient shown by the depths of the 20°C isotherm. Off the equator, the mean currents are in approximate geostrophic balance with the upper-layer thickness, as shown by the mean depths of the 20°C isotherm. The SEC is strongest at about 150°W and the NEC is strongest between 160°E and 160°W, where the north-south slopes of isotherm depths are largest. The NECC is strongest in the west Pacific, where the depth gradient associated with the counter-current trough is well defined and the EUC is weak due to a relatively flat east-west gradient. Sample flow trajectories over the annual cycle, following the depth of the 20°C isotherm (Fig. 25-27) show that starting within a few degrees of the equator all flow is eastward, while trajectories from 6°S also may converge onto the equator.

Zonal component of the horizontal current and its standard deviation (Figs. 28-31) are

much stronger than the meridional component everywhere, except at the western boundary where a strong subsurface current flows northwest along New Guinea (Lindstrom *et al.* 1987) and southward along Mindanao (Lukas 1988, Masumoto and Yamagata 1991). In these regions the annual cycle of the zonal component accounts for only a small portion of the total variance. The mean annual cycle is largely associated with the ITCZ. The NECC and NEC are strongest in the boreal winter, while the SEC is strongest in the boreal summer, consistent with the measurements of Wyrtki (1974) and Taft and Kessler (1991). In the east Pacific, the EUC spring surge is evident in the harmonic dials, although it accounts for only a small fraction of the total variance.

The equatorial zonal velocity (Fig. 29) shows that the deeper EUC west of 150°W is strongest in August, due to the strong zonal pressure gradient at that time. In the eastern Pacific, where the EUC is shallower, its strengthening in March-April is caused by relaxing trades (Lukas 1986). The SEC is shown by the westward flow above the EUC. The north-south section of zonal flow at 160°W shows the narrow meridional range of the EUC.

Meridional velocities, zonally averaged across the entire basin, are time averaged within seasons (Fig. 32-33). Near the surface the easterly wind stress forces poleward Ekman flows, with geostrophic return flows below the surface flows. During the boreal winter the influence of stronger northeast trades is seen by the broader northward flow away from the equator. The standard deviation during the boreal winter season is also larger at depth just north of the equator. In the boreal summer the southeast trades are stronger near and just north of the equator. Thus, there is strong northward flow just north of the equator, but it does not extend further north than

the southeast trades. In the Southern Hemisphere, the southward flow is strongest during the boreal summer. The maximum variance during boreal summer is at the surface just north of the equator, related to variance in the mean summer position of the ITCZ. Below about 50 m the flow is in the opposite direction, showing that on average vertical velocity near the equator should be largest near that depth.

Vertical velocity at 50 m (Fig. 34) is computed using the horizontal velocities and the assumption of non-divergent flow. It shows strong organized mean upwelling along the equator, where the standard deviation is also largest. Away from the equator the vertical velocity is relatively weak, except along the western boundary where it is more noisy. The annual cycle accounts for relatively little variance in vertical velocity, and is not shown here. Uncertainties in the vertical velocity are related to uncertainties in the horizontal velocities from which it is computed. The magnitude of the equatorial Pacific vertical velocity is comparable to observations (e.g., Wyrtki 1981b Bryden and Brady 1985).

Acknowledgements: We thank the Coupled Model Project of NMC, particularly A. Leetmaa, D. Behringer, M. Ji, R. Reynolds, and M. Ji for supplying the data and for many suggestions. We are also grateful to C. Ropelewski, X. Wang, and V. Kousky for discussions. Part of this research has been supported by the Equatorial Pacific Ocean Climate Studies (EPOCS) program.

References

Bryan, K., 1969: A numerical method for the study of the World Ocean. *J. Comput. Phys.*, **4**, 347-376.

Bryden, H.L., and E.C. Brady, 1985: Diagnostic model of the three-dimensional circulation in the upper equatorial Pacific Ocean. *J. Phys. Oceanogr.*, **15**, 1255-1273.

Cox, M.D., 1984: A primitive, 3-dimensional model of the ocean. GFDL Ocean Group Tech. Rep. No. 1, Geophysical Fluid Dynamics Laboratory, 143 pp.

Derber, J., and A. Rosati, 1989: A global oceanic data assimilation system. *J. Phys. Oceanogr.*, **19**, 1333-1347.

Halpert, M.S., and C.F. Ropelewski, 1989: *Atlas of Tropical Sea Surface Temperature and Surface Winds.* NOAA Atlas No. 8, U.S. Govt. Printing Office 1989-242-312/04048, 13 pp + 150 figs.

Harrison, D.E., 1989: On climatological monthly mean wind stress and wind stress curl fields over the world ocean. *J. Climate*, **2**, 57-70.

Hayes, S.P., L.J. Mangum, J. Picaut, A. Sumi, and K. Takeuchi, 1991: TOGA-TAO: a moored array for real-time measurements in the tropical Pacific Ocean. *Bull. Amer. Meteor. Soc.*, **72**, 339-347.

Hellerman, S., and M. Rosenstein, 1983: Normal monthly wind stress over the world ocean with error estimates. *J. Phys. Oceanogr.*, **13**, 1093-1104.

Horel, J.D., 1982: On the annual cycle of the tropical Pacific atmosphere and ocean. *Mon. Wea. Rev.*, **110**, 1863-1878.

Ji, M., A. Leetmaa, and J. Derber, 1994a: An ocean analysis system for climate studies. Submitted to *Mon. Wea. Rev.*

Ji, M., A. Kumar, and A. Leetmaa, 1994b: An experimental coupled forecast system at the National Meteorological Center: some early results. In press, *Tellus.*

Kessler, W.S., and B.A. Taft, 1987: Dynamic heights and zonal geostrophic transports in the central Pacific 1979-1984. *J. Phys. Oceanogr.*, **17**, 97-122.

Kousky, V.E., and A. Leetma, 1989: The 1986-87 Pacific warm episode: Evolution of oceanic and atmospheric anomaly fields. *J. Climate*, **2**, 254-267.

Leetmaa, A., and M. Ji, 1989: Operational hindcasting of the tropical Pacific. *Dyn. Atmos. Oceans*, **13**, 465-490.

Levitus, S., 1982: *Climatological Atlas of the World Ocean*. NOAA Prof. Paper 13, U.S. Govt. Printing Office, Washington, DC, 173 pp.

Levitus, S., and R.D. Gelfeld, 1992: *National Oceanographic Data Center Inventory of Physical Oceanographic Profiles, Global Distributions by Year for All Countries*, 242 pp. U.S. Dept. of Commerce/NOAA. NODC user services branch, NOAA/NESDIS E/OC21, Washington, DC, 20235.

Lindstrom, E., R. Lukas, R. Fine, E. Firing, S. Godfrey, G. Meyers, and M. Tsuchiya, 1987: The western equatorial Pacific Ocean circulation study. *Nature*, **330**, 533-537.

Lukas, R., 1986: The termination of the Equatorial Undercurrent in the eastern Pacific. *Prog. Oceanogr.*, **16**, 63-90.

Lukas, R., 1988: Interannual fluctuations of the Mindanao Current inferred from sea level. *J. Geophys. Res.*, **93**, 6744-6748.

Masumoto, Y., and T. Yamagata, 1991: Response of the western tropical Pacific to the Asian winter monsoon: The generation of the Mindanao Dome. *J. Phys. Oceanogr.*, **21**, 1386-1398.

Meehl, G.A., 1987: The annual cycle and interannual variability in the tropical Pacific and Indian Ocean regions. *Mon. Wea. Rev.*, **115**, 27-50.

Oberhuber, J.M., 1988: *An atlas basen on the 'COADS' data set: the budgets of heat, buoyancy and turbulent kinetic energy at the surface of the global ocean.* Report No. 15, Max-Plank-Institude fur Meteorologie, 2000 Hamburg 13, Bundesstrasse 55, FRG.

Philander, S.G.H., W.J. Hurlin, and A.D. Seigel, 1987: Simulation of the seasonal cycle of the tropical Pacific Ocean. *J. Phys. Oceanogr.*, **17**, 1986-2002.

Reynolds, R.W., and D.C. Marsico, 1993: An improved real-time global sea surface temperature analysis. *J. Climate*, **6**, 114-119.

Reynolds, R.W., and T.M. Smith, 1993: Improved global sea surface temperature analysis using optimum interpolation. Submitted to *J. Climate*.

Shea, D.J., K.E. Trenberth, and R.W. Reynolds, 1992: A global monthly sea surface temperature climatology. *J. Climate*, **5**, 987-1001.

Taft, B.A., and W.S. Kessler, 1991: Variations of zonal currents in the central tropical Pacific during 1970 to 1987: sea level and dynamic height measurements. *J. Geophys. Res.*, **96**, 12599-12618.

Wyrtki, K., 1974: Equatorial currents in the Pacific 1950 to 1970 and their relations to the trade winds. *J. Phys. Oceanogr.*, **4**, 372-380.

Wyrtki, K., E. Firing, D. Halpern, R. Knox, G.J. McNally, W.C. Patzert, E.D. Stroup, B.A. Taft, and R. Williams, 1981a: The Hawaii to Tahiti shuttle experiment. *Science*, **211**, 22-28.

Wyrtki, K., 1981b: An estimate of equatorial upwelling in the Pacific. *J. Phys. Oceanogr.*, **11**, 1205-1214.

LIST OF FIGURES

Data, Analysis, and Validation

The Air-Sea Interface

Temperature Cross Sections

Fig. 8. The longitude-depth section of temperature (°C) at 10°S, ten-year mean and monthly standard deviation (a). Shading for standard deviations > 1°C (light), 2°C (medium), and 3°C (dark). Annual cycle harmonic dials and the percent variance accounted for by the annual cycle (b). Medium shading for > 30% variance accounted, dark shading for > 60%. The reference vector has units of °C, otherwise as in Fig. 3.

Fig. 9. The latitude-depth section of temperature (°C) at 165°E, ten-year mean and monthly standard deviation (a). Shading for standard deviations > 1°C (light), 2°C (medium), and 3°C (dark). Annual cycle harmonic dials and the percent variance accounted for by the annual cycle (b). Medium shading for > 30% variance accounted, dark shading for > 60%. The reference vector has units of °C, otherwise as in Fig. 3.

Fig. 10. The latitude-depth section of temperature (°C) at 160°W ten-year mean and monthly standard deviation (a). Shading for standard deviations > 1°C (light), 2°C (medium), and 3°C (dark). Annual cycle harmonic dials and the percent variance due to the annual cycle (b). Medium shading for > 30% variance accounted, dark shading for > 60%. The reference vector has units of °C, otherwise as in Fig. 3.

Fig. 11. The latitude-depth section of temperature (°C) at 110°W, ten-year mean and monthly standard deviation (a). Shading for standard deviations > 1°C (light), 2°C (medium), and 3°C (dark). Annual cycle harmonic dials and the percent variance due to the annual cycle (b). Medium shading for > 30% variance accounted, dark shading for > 60%. The reference vector has units of °C, otherwise as in Fig. 3.

Fig. 12. The longitude-depth section of temperature (°C) at 10°N, seasonal mean and monthly standard deviation using all December-February months in the ten-year record (a). As in (a) except using all March-May months (b). Shading for standard deviations > 1°C (light), 2°C (medium), and 3°C (dark).

Fig. 13. The longitude-depth section of temperature (°C) at 10°N, seasonal mean and monthly standard deviation using all June-August months in the ten-year record (a). As in (a) except using all September-November months (b). Shading for standard deviations > 1°C (light), 2°C (medium), and 3°C (dark).

Fig. 14. The longitude-depth section of temperature at the equator (°C), seasonal mean and monthly standard deviation (a) using all December-February months in the ten-year record. As in (a) except using all March-May months (b). Shading for standard deviations > 1°C (light), 2°C (medium), and 3°C (dark).

Fig. 15. The longitude-depth section of temperature (°C) at the equator, seasonal mean and monthly standard deviation using all June-August months in the ten-year record (a). As in (a) except using all September-November months (b). Shading for standard deviations > 1°C (light), 2°C (medium), and 3°C (dark).

Depths of the 20°C Isotherm

Fig. 16. The depth (m) of the 20°C isotherm ten-year mean and monthly standard deviation (a). Shading for standard deviations > 15 m (light), 20 m (medium), and 25 m (dark). Annual cycle harmonic dials and the percent variance due to the annual cycle (b). Medium shading for > 30% variance accounted, dark shading for > 60%. The reference vector has units of meters, otherwise as in Fig. 3.

Fig. 17. The depth (m) of the 20°C isotherm, seasonal mean and monthly standard deviation (a) using all December-February months in the ten-year record. As in (a) except using all March-May months (b). Shading for standard deviations > 15 m (light), 20 m (medium), and 25 m (dark).

Fig. 18. The depth (m) of the 20°C isotherm seasonal mean and monthly standard deviation using all June-August months in the ten-year record (a). As in (a) except using all September-November months (b). Shading for standard deviations > 15 m (light), 20 m (medium), and 25 m (dark).

Fig. 19. Time-longitude of the annual cycle of the 20°C isotherm along 10°S, the equator, and 10°N, in meters. Depths greater than 150 m are shaded.

Fig. 20. Time-latitude of the annual cycle of the 20°C isotherm along 165°E, 160°W, and 110°W, in meters. Depths greater than 150 m are shaded.

Subsurface Horizontal Temperature Variations

Fig. 21. The average temperature (°C) over the upper 200 m, ten-year mean and monthly standard deviation (a). Shading for standard deviations > 1°C (light), 2°C (medium), and 3°C (dark). Annual cycle harmonic dials and the percent variance due to the annual cycle (b). Medium shading for > 30% variance accounted, dark shading for > 60%. The reference vector has units of °C, otherwise as in Fig. 3.

Fig. 22. The temperature (°C) at 100 m, ten-year mean and monthly standard deviation (a). Shading for standard deviations > 1°C (light), 2°C (medium), and 3°C (dark). Annual cycle harmonic dials and the percent variance due to the annual cycle (b). Medium shading for > 30% variance accounted, dark shading for > 60%. The reference vector has units of °C, otherwise as in Fig. 3.

Fig. 23. The temperature (°C) at 200 m, ten-year mean and monthly standard deviation (a). Shading for standard deviations > 1°C (light), 2°C (medium), and 3°C (dark). Annual cycle harmonic dials and the percent variance due to the annual cycle (b). Medium shading for > 30% variance accounted, dark shading for > 60%. The reference vector has units of °C, otherwise as in Fig. 3.

Ocean Currents

Fig. 24. Horizontal velocity (m s^{-1}) averaged from the surface to 200 meters, ten-year mean and monthly standard deviation. Shading for standard deviations > 0.1 m s^{-1} (light), 0.2 m s^{-1} (medium), and 0.3 m s^{-1} (dark). Zonal velocity annual cycle harmonic dials and percent variance due to the annual cycle (b). Medium shading for > 30% variance accounted, dark shading for > 60%. The reference vector has units of m s^{-1}, otherwise as in Fig. 3.

Fig. 25. Trajectories of water flow along the depth of the 20°C isotherm over the annual cycle for parcels starting at 3°S, the equator, and 3°N. Starting locations, for January, are shown by the crosses.

Fig. 26. Trajectories of water flow along the depth of the 20°C isotherm over the annual cycle for parcels starting at 6°S, 9°S, and 12°S. Starting locations, for January, are shown by the crosses.

Fig. 27. Trajectories of water flow along the depth of the 20°C isotherm over the annual cycle for parcels starting at 6°N, 9°N, and 12°N. Starting locations, for January, are shown by the crosses.

Fig. 28. Ten-year mean and monthly standard deviation of zonal velocity (m s^{-1}) at 100 m (a). Shading for standard deviations > 0.1 m s^{-1} (light), 0.2 m s^{-1} (medium), and 0.3 m s^{-1} (dark). The contour interval is 0.2, except that the ± 0.1 contours are also shown. Zonal velocity annual cycle harmonic dials and percent variance due to the annual cycle (b). Medium shading for > 30% and dark shading for > 60% explained variance. The reference vector has units of m s^{-1}, otherwise as in Fig. 3.

Fig. 29. Ten-year mean and monthly standard deviation of zonal velocity (m s^{-1}) at 200 m (a). Shading for standard deviations > 0.1 m s^{-1} (light), 0.2 m s^{-1} (medium), and 0.3 m s^{-1} (dark). The contour interval is 0.2, except that the ± 0.1 contours are also shown. Zonal velocity annual cycle harmonic dials and percent variance due to the annual cycle (b). Medium shading for > 30% and dark shading for > 60% explained variance. The reference vector has units of m s^{-1}, otherwise as in Fig. 3.

Fig. 30. The longitude-depth section of zonal velocity on the equator (m s^{-1}) ten-year mean and monthly standard deviation (a). Shading for standard deviations > 0.3 m s^{-1} (light), 0.35 m s^{-1} (medium), and 0.4 m s^{-1} (dark). Zonal velocity annual cycle harmonic dials and percent variance due to the annual cycle (b). Medium shading for > 30% and dark shading for > 60% explained variance. The reference vector has units of m s^{-1}, otherwise as in Fig. 3.

Fig. 31. The zonal velocity (m s^{-1}) at 160°W ten-year mean and monthly standard deviation (a). Shading for standard deviations > 0.1 m s^{-1} (light), 0.2 m s^{-1} (medium), and 0.3 m s^{-1} (dark). Zonal velocity annual cycle harmonic dials and percent variance due to the annual cycle (b). Medium shading for > 30% and dark shading for > 60% explained variance. The reference vector has units of m s^{-1}, otherwise as in Fig. 3.

Fig. 32. The zonal average of meridional velocity (10^{-2} m s^{-1}) seasonal mean and monthly standard deviation using all December-February months in the ten-year record (a). As in (a) except using all March-May months (b). Shading for standard deviations > 1 10^{-2} m s^{-1} (light), 2 10^{-2} m s^{-1} (medium), and 3 10^{-2} m s^{-1} (dark).

Fig. 33. The zonal average of meridional velocity (10^{-2} m s^{-1}) seasonal mean and monthly standard deviation using all June-August months in the ten-year record (a). As in (a) except using all September-November months (b). Shading for standard deviations > $1x10^{-2}$ m s^{-1} (light), $2x10^{-2}$ m s^{-1} (medium), and $3x10^{-2}$ m s^{-1} (dark).

Fig. 34. Vertical velocity at 50 m depth (10^{-5} m s^{-1}) ten-year mean and monthly standard deviation. The contour interval is $1x10^{-5}$ m s^{-1}, except that the ± $0.5x10^{-5}$ m s^{-1} contour is also shown and the zero contour is omitted. Shading for standard deviations > $1x10^{-5}$ m s^{-1} (light), $2x10^{-5}$ m s^{-1} (medium), and $3x10^{-5}$ m s^{-1} (dark).

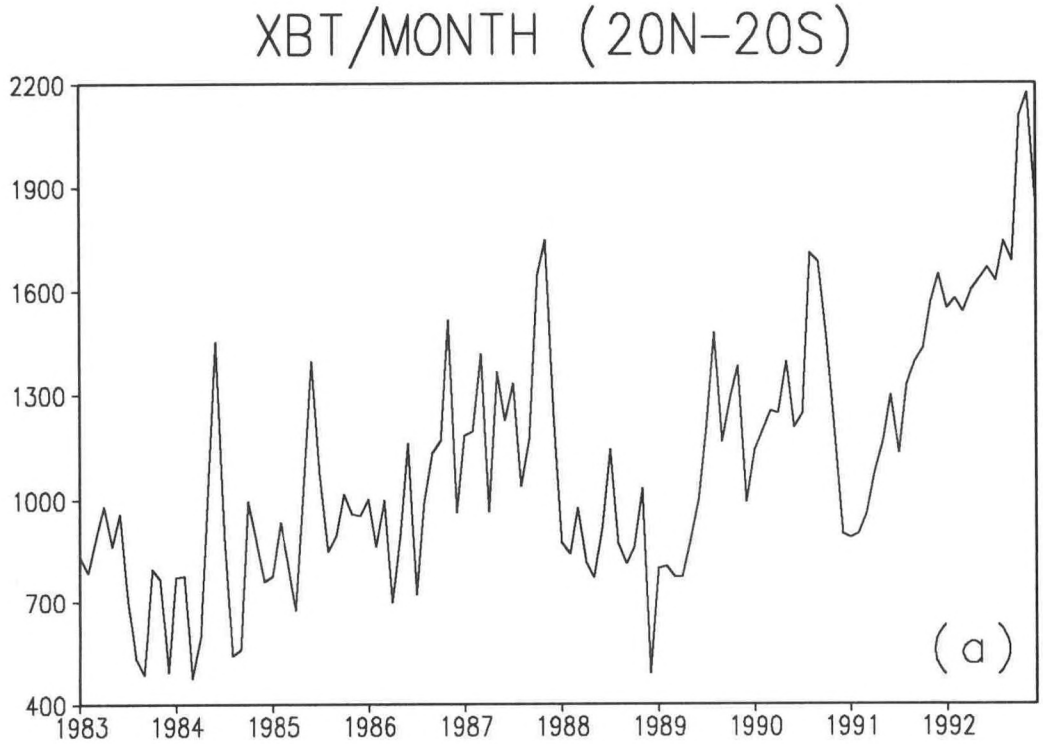

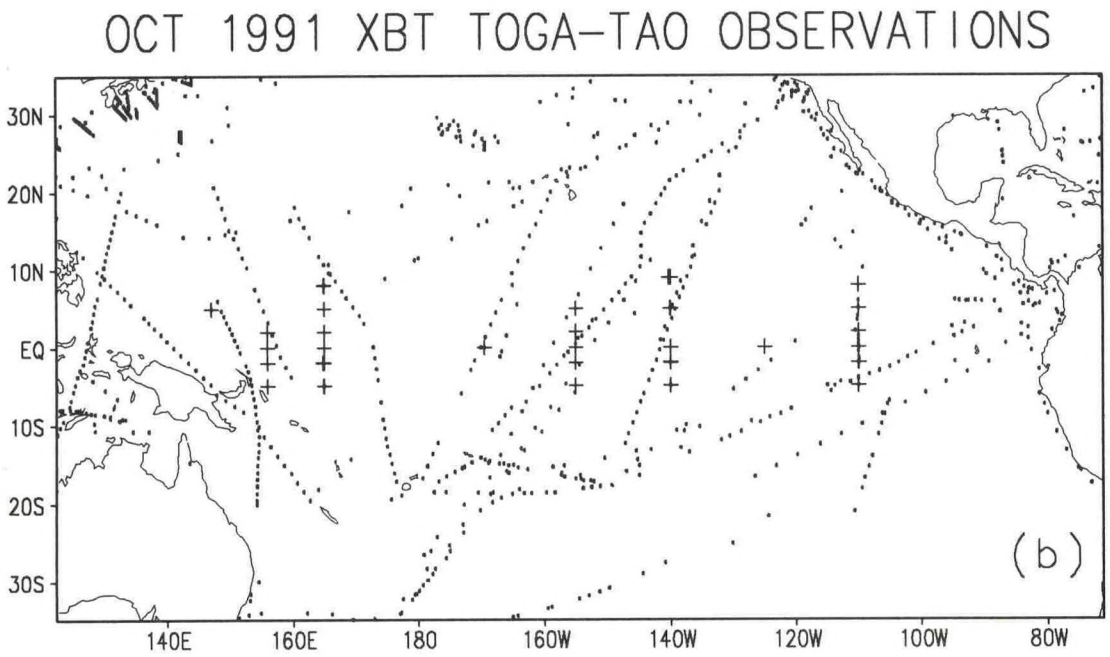

Fig. 1. Number of XBT observations per month in the Pacific Ocean between 20°N and 20°S (a) and the distribution of XBT (dots) and moored buoy (crosses) subsurface temperature observations for the month of October 1991.

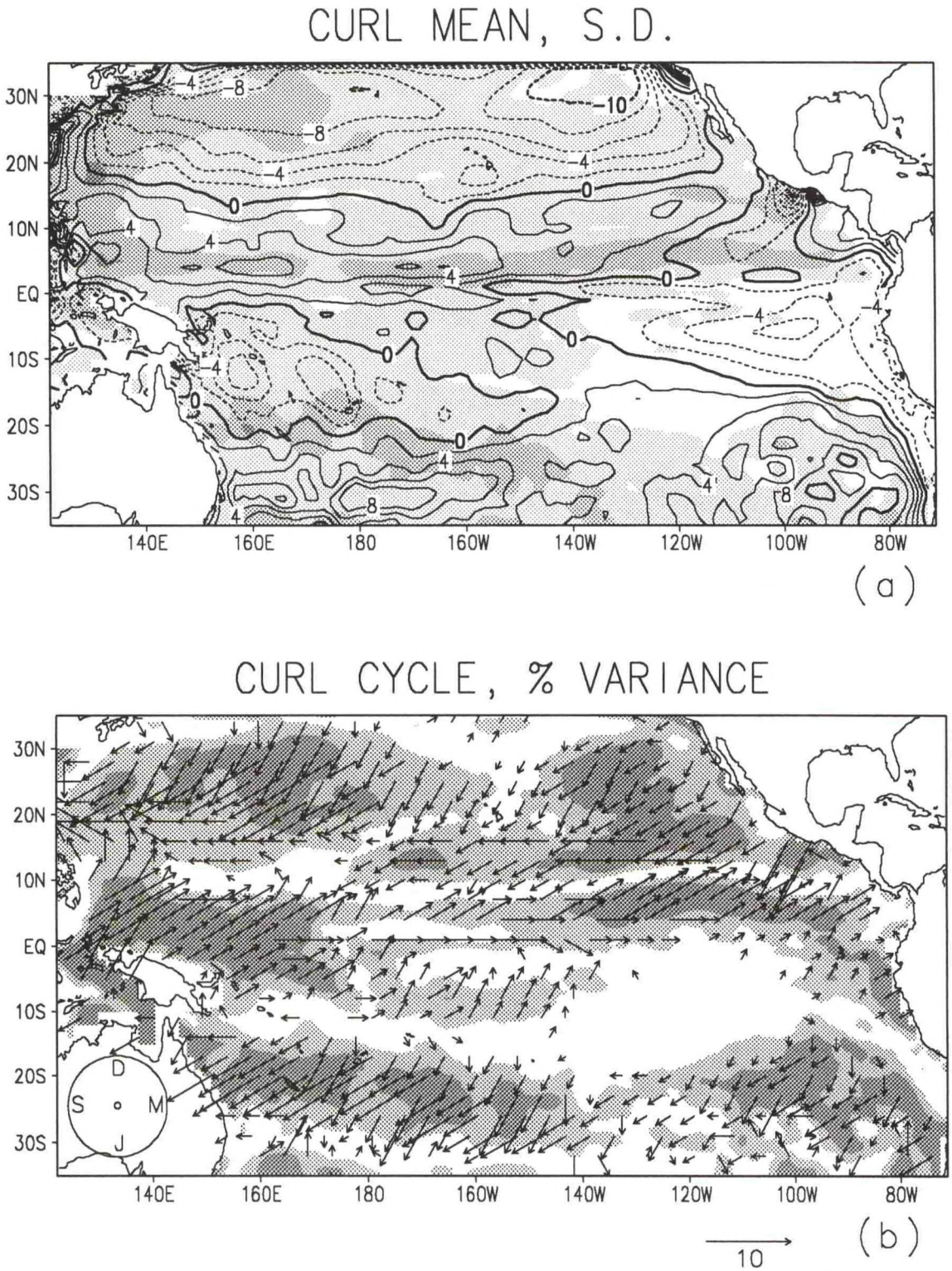

Fig. 2. The $Curl_z\tau$ (10^{-8} N m^{-3}) mean and monthly standard deviation (a) over the 10 year period. Shading shows standard deviations > $2x10^{-8}$ Nm^{-3} (light), $4x10^{-8}$ Nm^{-3} (medium), and $6x10^{-8}$ Nm^{-3} (dark). Annual cycle harmonic vectors and percent variance explained by the annual cycle (shading) (b). More than 30% variance accounted is medium shading, more than 60% accounted is dark shading. Harmonic dials show the annual cycle (direction) and amplitude (length). The legend at the lower left shows when the annual cycle is maximum (Dec. at 12 o'clock, Mar at 3 o'clock, etc.) and the reference vector at the lower right scales the amplitude.

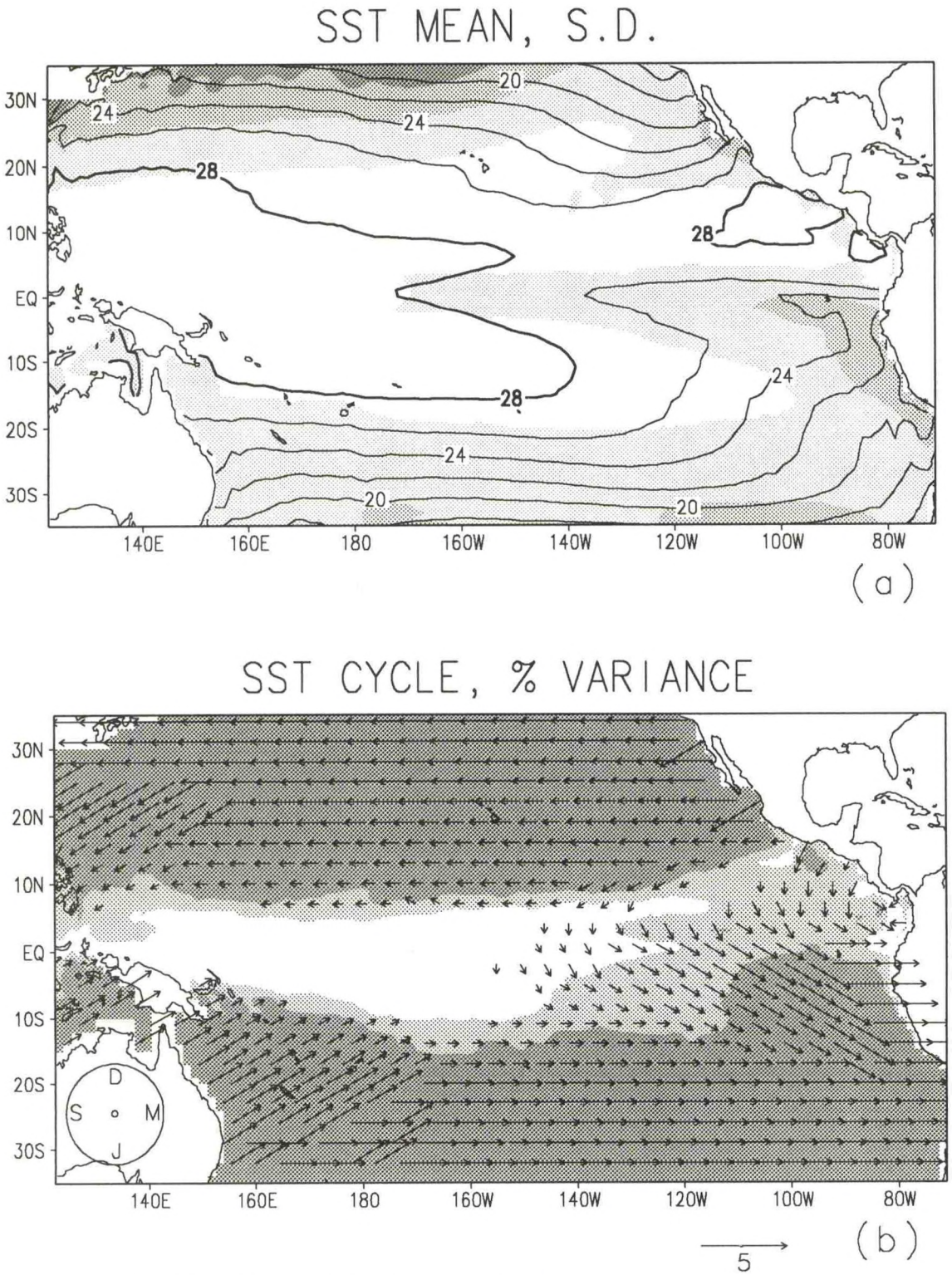

Fig. 3. The SST (°C) ten-year mean and monthly standard deviation (a). Shading for standard deviations > 1°C (light), 2°C (medium), and 3°C (dark). Annual cycle harmonic dials and the percent variance accounted for by the annual cycle (b). Medium shading for > 30% variance accounted, dark shading for > 60%. The reference vector has units of °C, otherwise as in Fig. 2.

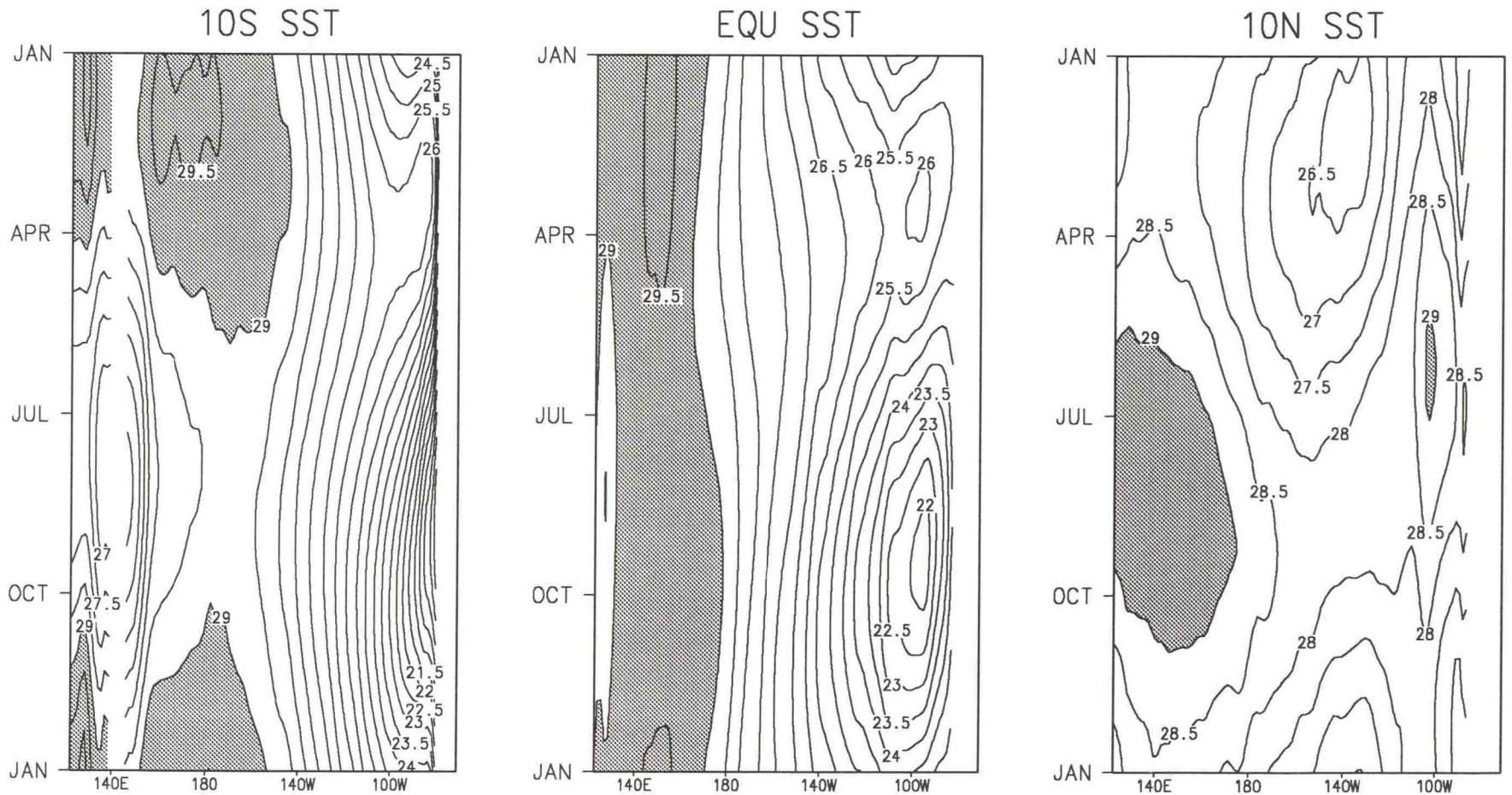

Fig. 4. Time-longitude of the annual cycle of SST (°C) at 10°S, the equator, and 10°N.

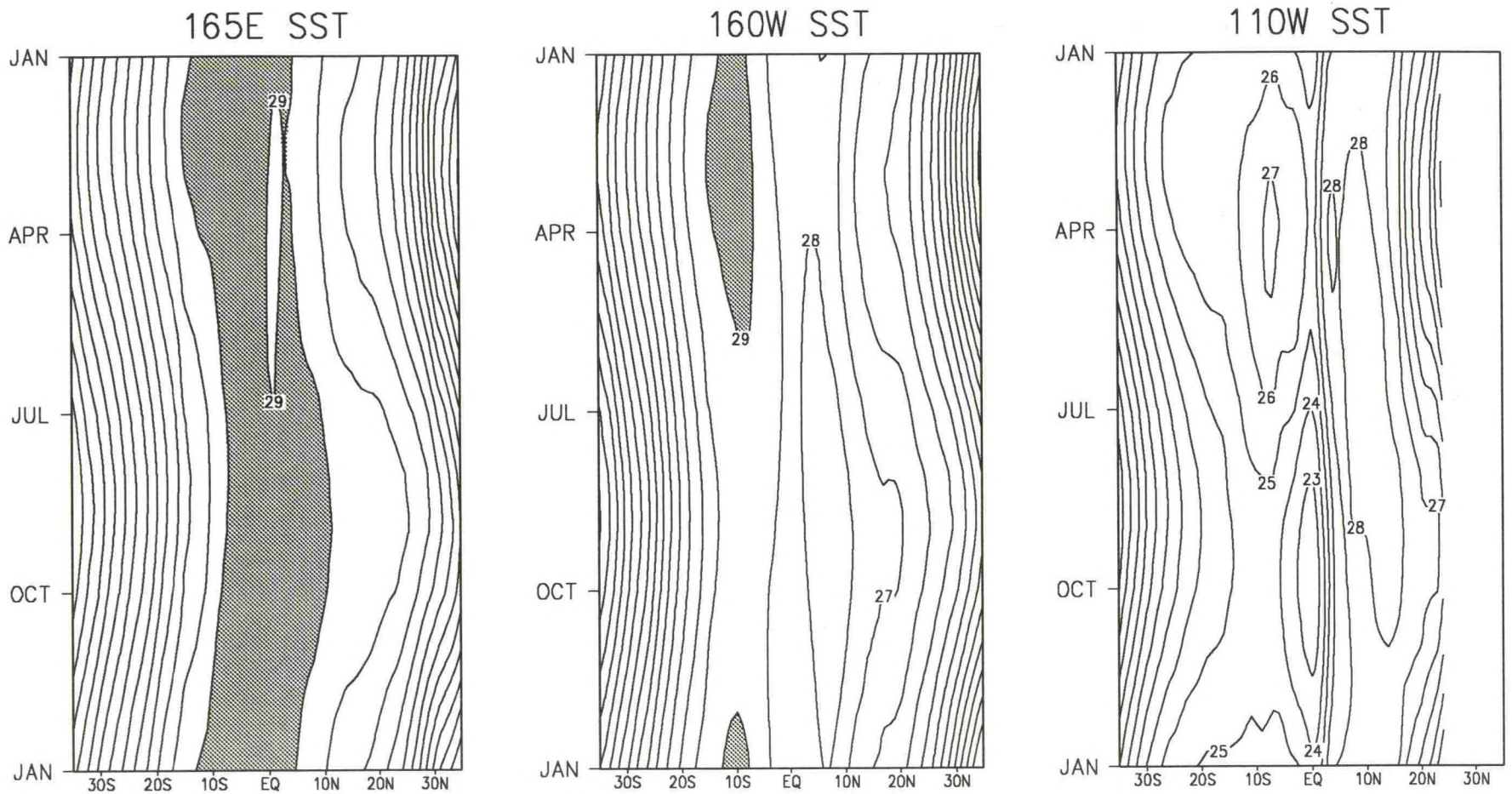

Fig. 5. Time-latitude of the annual cycle of SST (°C) at 165°E, 160°W, and 110°W .

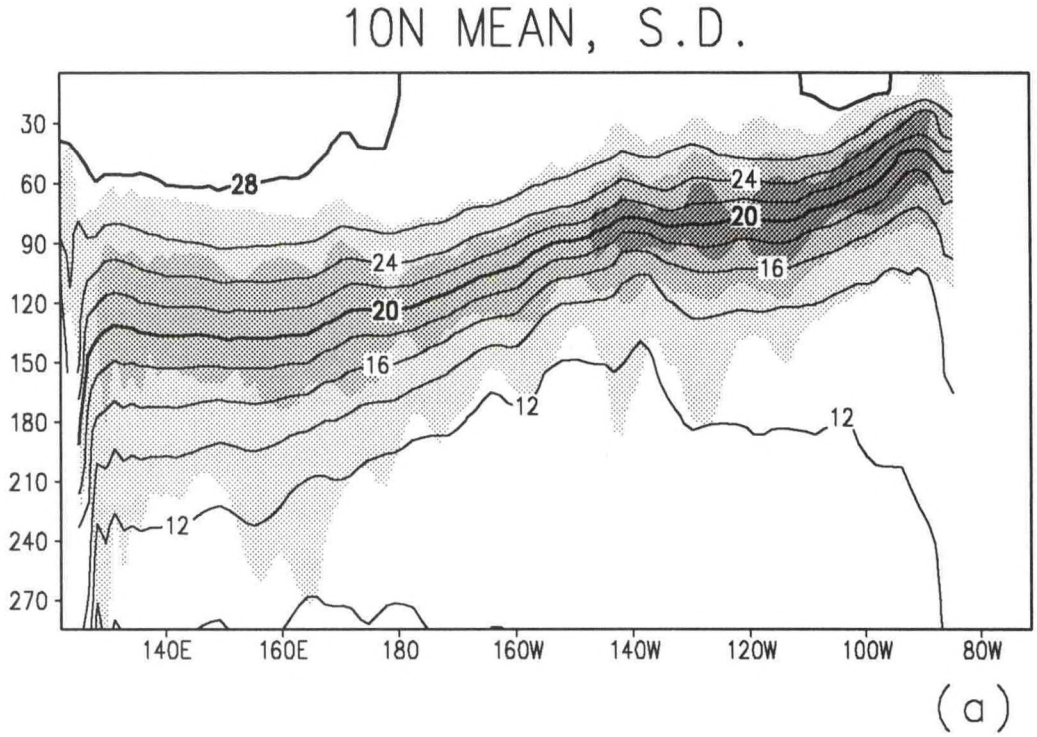

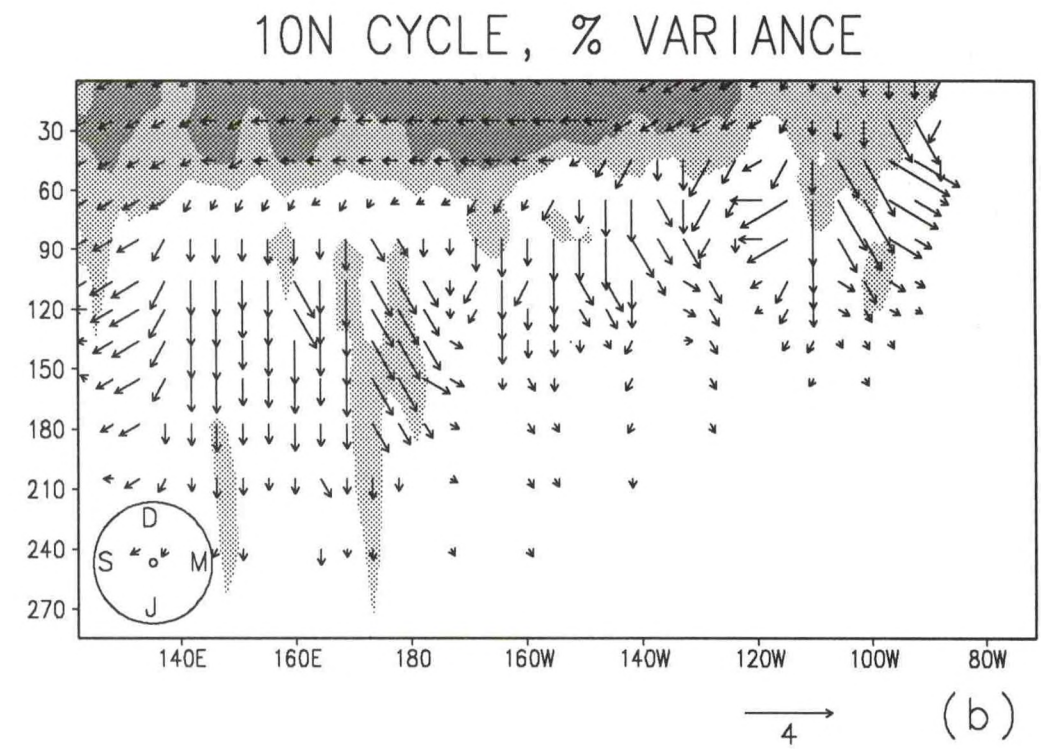

Fig. 6. The longitude-depth section of temperature (°C) at 10°N, ten-year mean and monthly standard deviation (a). Shading for standard deviations > 1°C (light), 2°C (medium), and 3°C (dark). Annual cycle harmonic dials and the percent variance explained by the annual cycle (b). Medium shading for > 30% variance accounted, dark shading for > 60%. The reference vector has units of °C, otherwise as in Fig. 2.

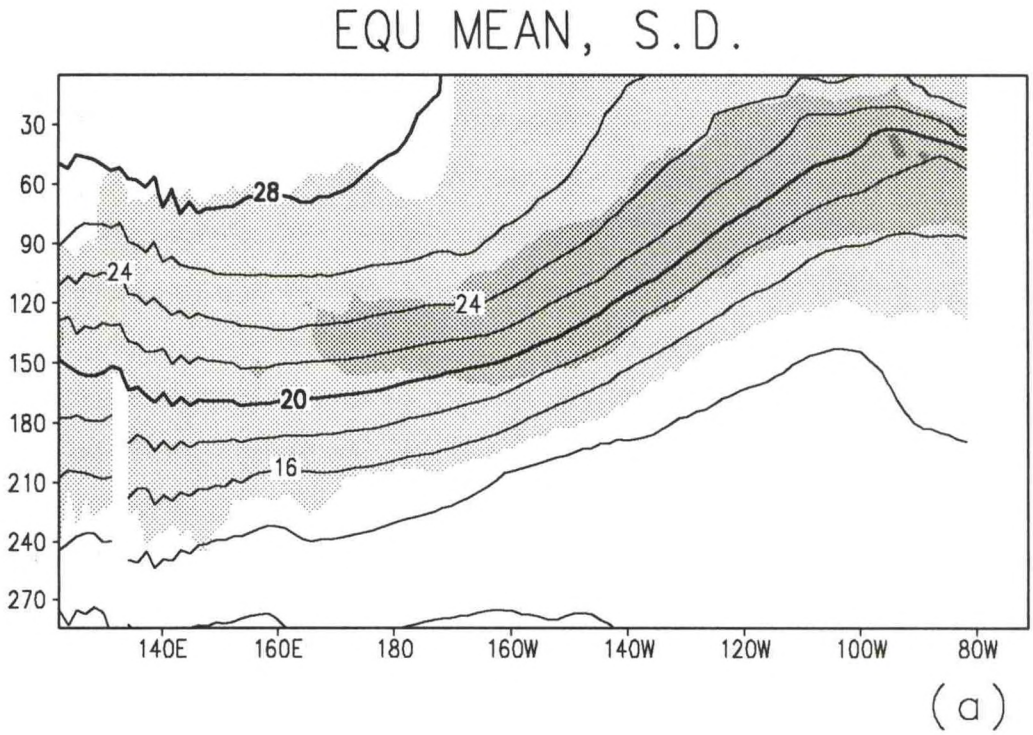

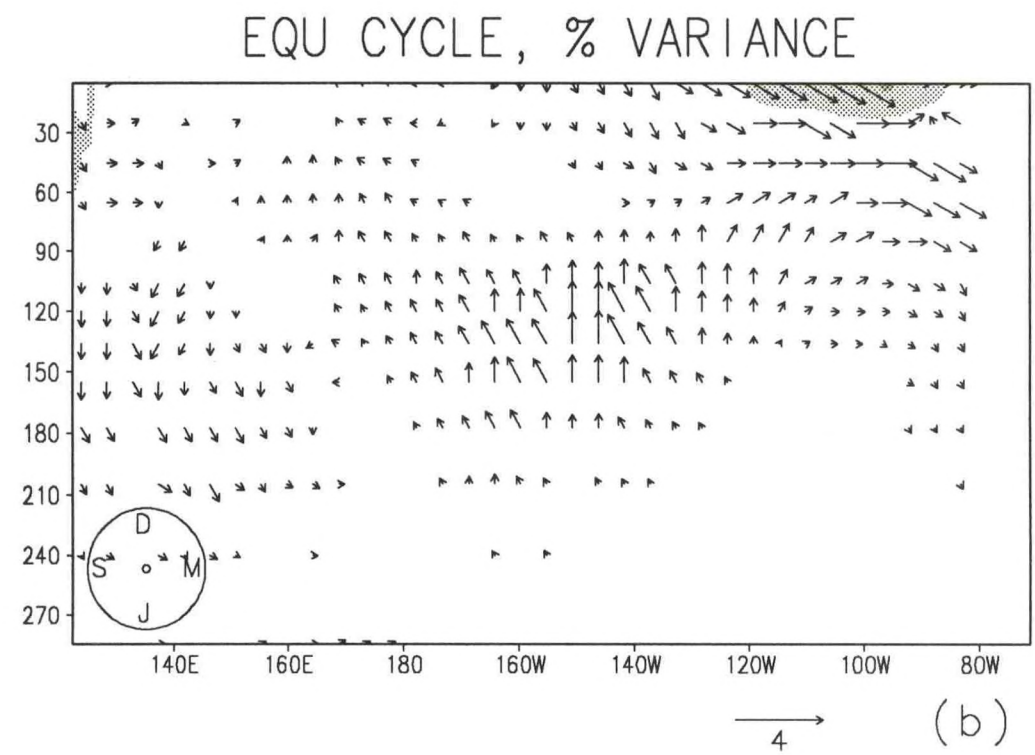

Fig. 7. The longitude-depth section of temperature (°C) at the equator ten-year mean and monthly standard deviation (a). Shading for standard deviations > 1°C (light), 2°C (medium), and 3°C (dark). Annual cycle harmonic dials and the percent variance explained by the annual cycle (b). Medium shading for > 30% variance accounted, dark shading for > 60%. The reference vector has units of °C, otherwise as in Fig. 2.

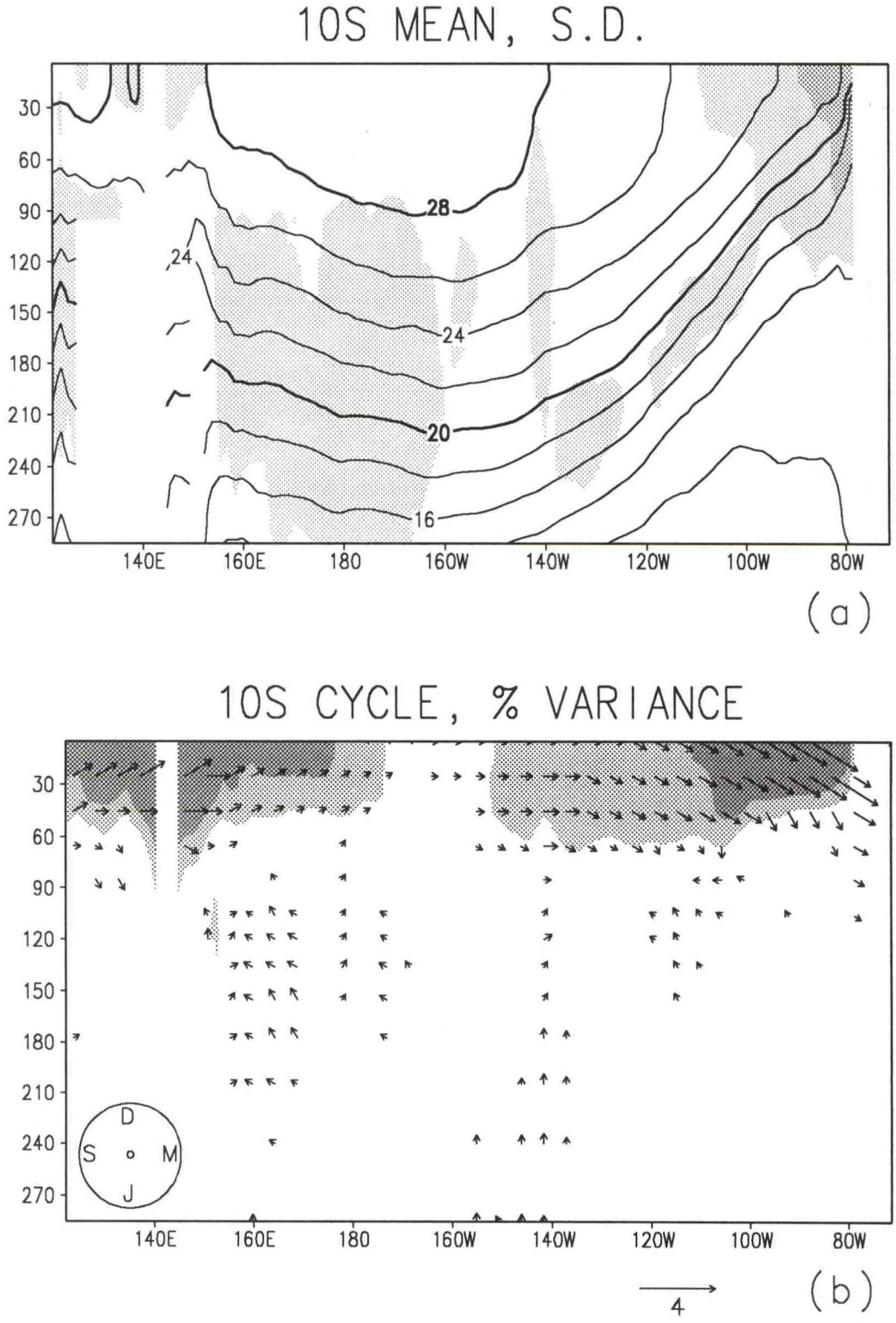

Fig. 8. The longitude-depth section of temperature (°C) at 10°S, ten-year mean and monthly standard deviation (a). Shading for standard deviations > 1°C (light), 2°C (medium), and 3°C (dark). Annual cycle harmonic dials and the percent variance accounted for by the annual cycle (b). Medium shading for > 30% variance accounted, dark shading for > 60%. The reference vector has units of °C, otherwise as in Fig. 2.

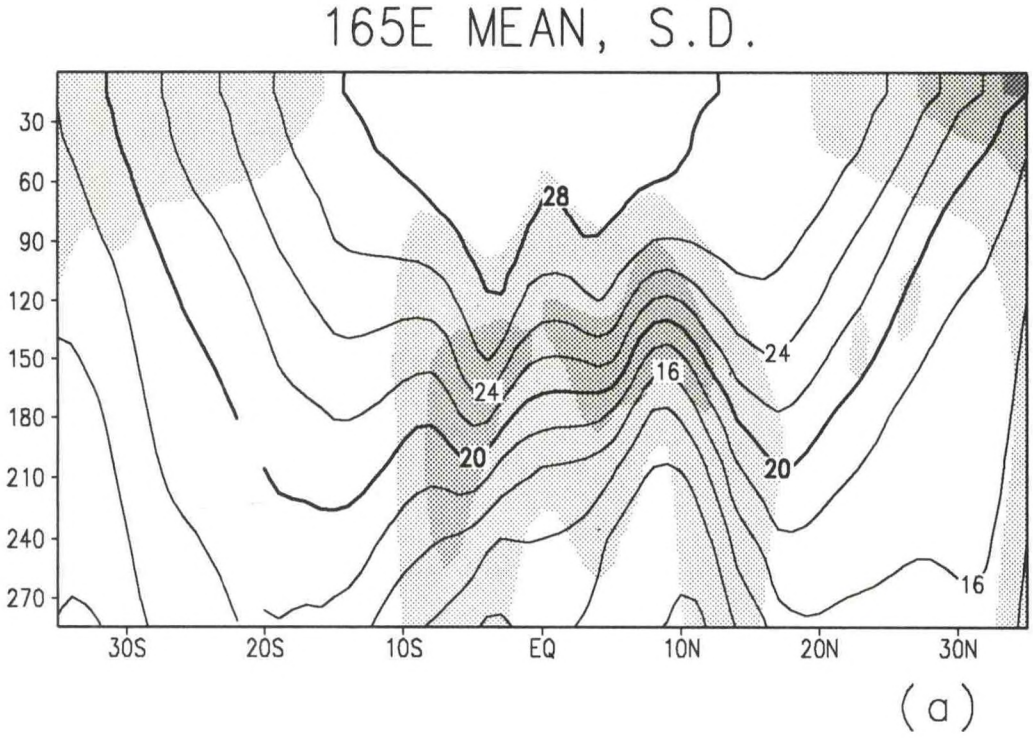

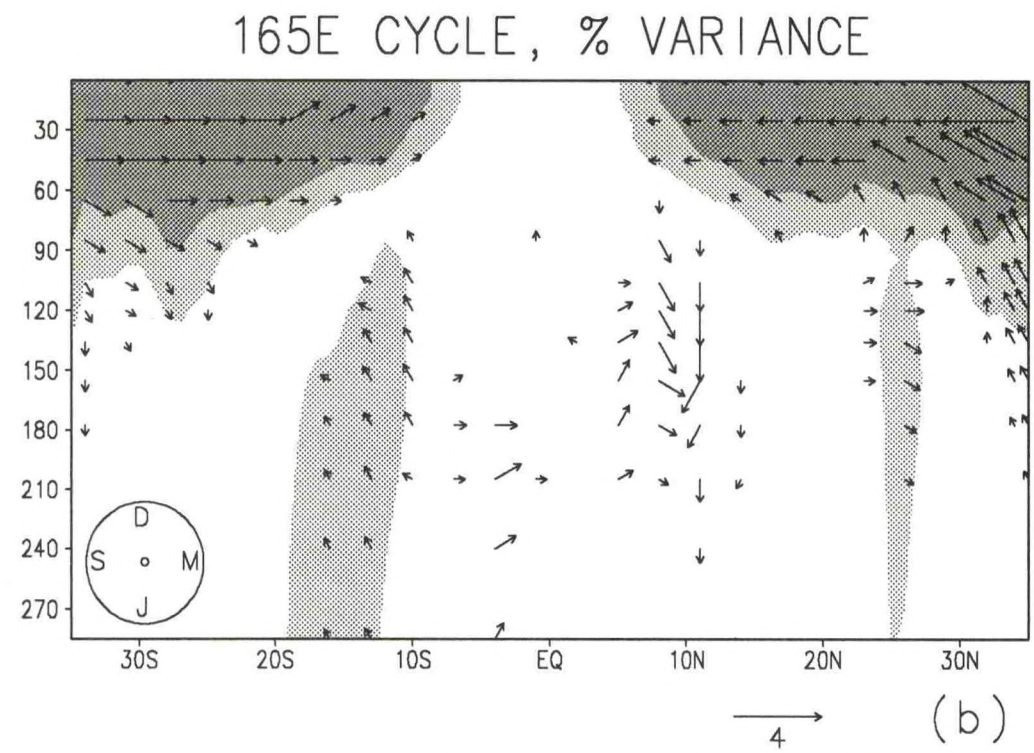

Fig. 9. The latitude-depth section of temperature (°C) at 165°E, ten-year mean and monthly standard deviation (a). Shading for standard deviations > 1°C (light), 2°C (medium), and 3°C (dark). Annual cycle harmonic dials and the percent variance accounted for by the annual cycle (b). Medium shading for > 30% variance accounted, dark shading for > 60%. The reference vector has units of °C, otherwise as in Fig. 2.

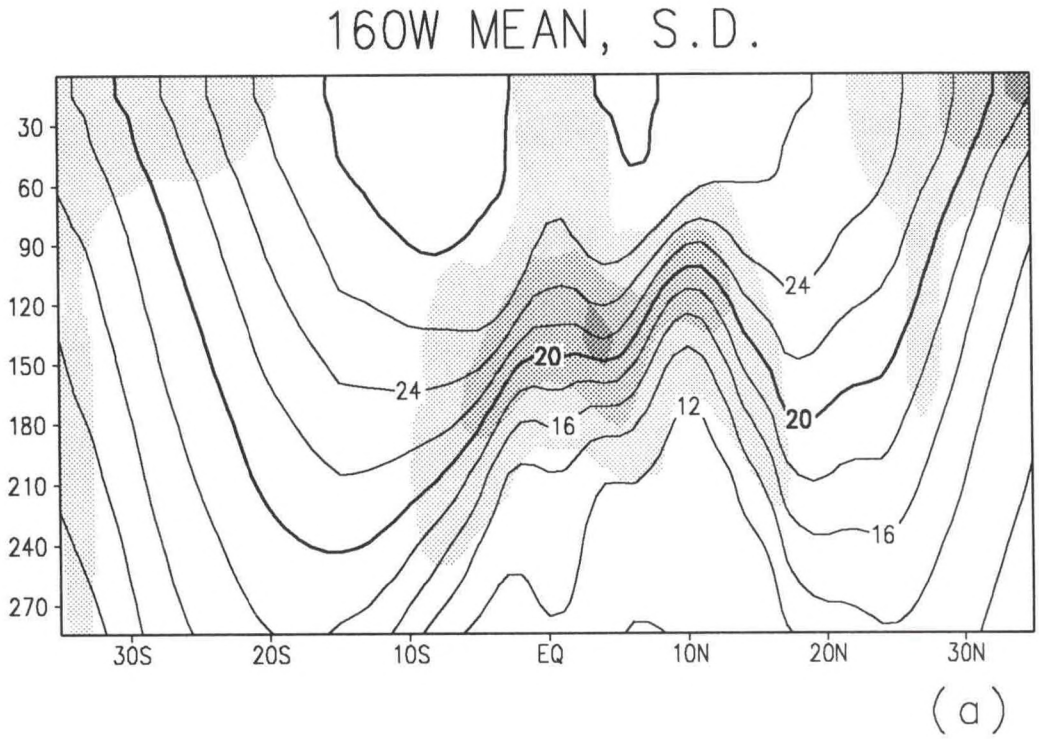

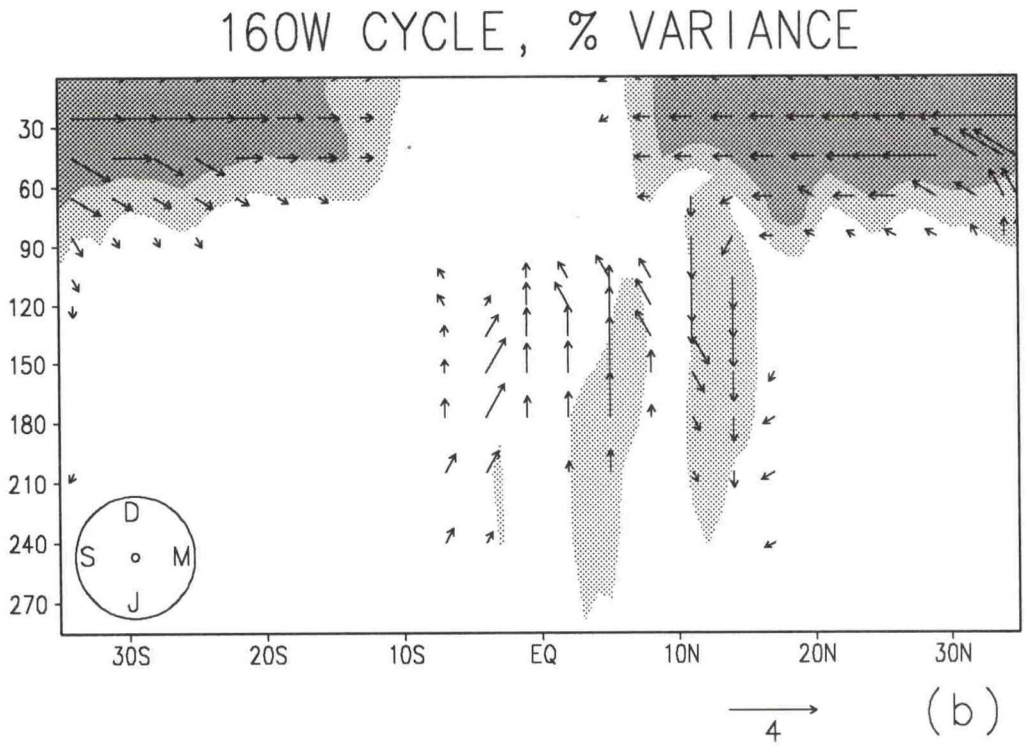

Fig. 10. The latitude-depth section of temperature (°C) at 160°W ten-year mean and monthly standard deviation (a). Shading for standard deviations > 1°C (light), 2°C (medium), and 3°C (dark). Annual cycle harmonic dials and the percent variance due to the annual cycle (b). Medium shading for > 30% variance accounted, dark shading for > 60%. The reference vector has units of °C, otherwise as in Fig. 2.

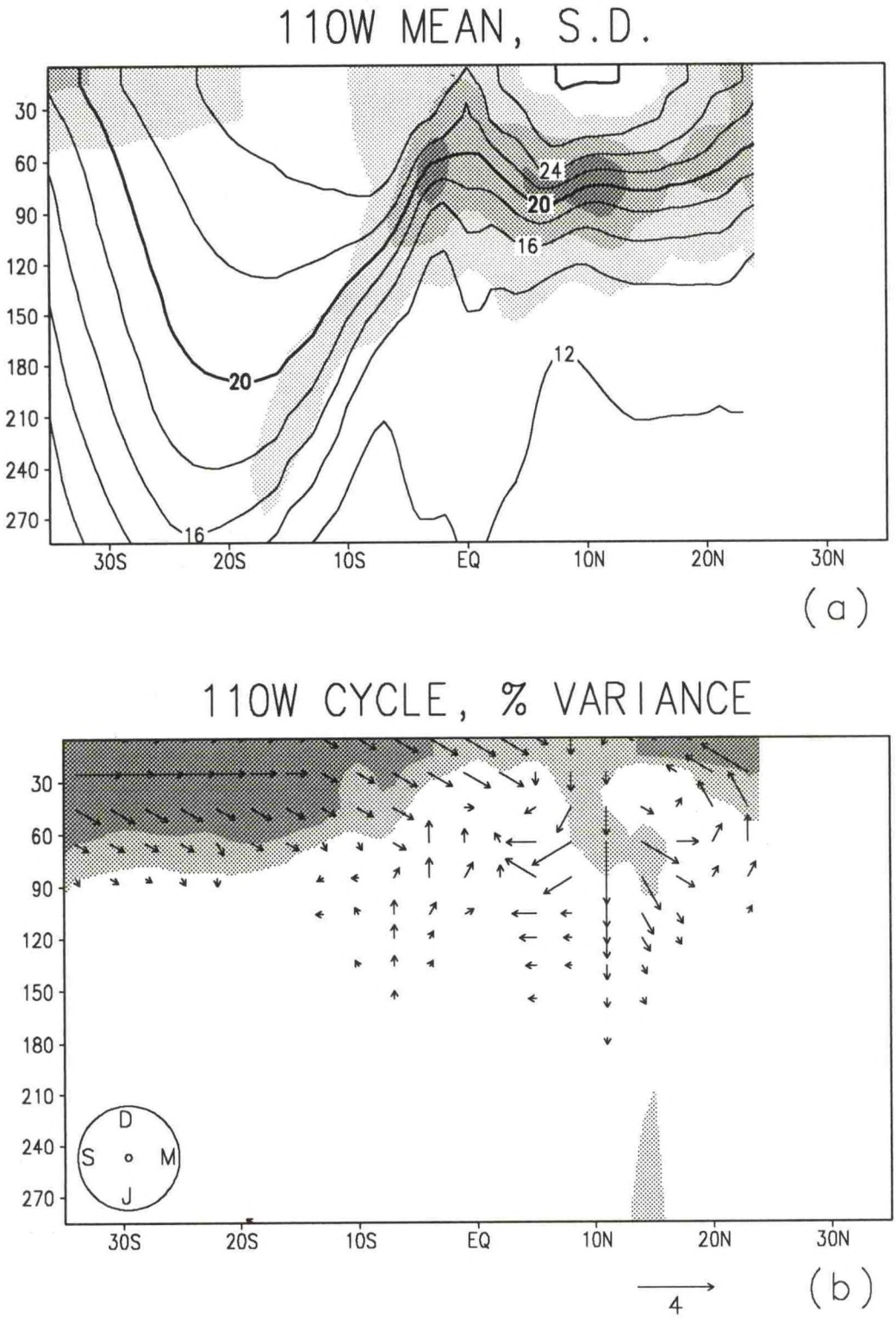

Fig. 11. The latitude-depth section of temperature (°C) at 110°W, ten-year mean and monthly standard deviation (a). Shading for standard deviations > 1°C (light), 2°C (medium), and 3°C (dark). Annual cycle harmonic dials and the percent variance due to the annual cycle (b). Medium shading for > 30% variance accounted, dark shading for > 60%. The reference vector has units of °C, otherwise as in Fig. 2.

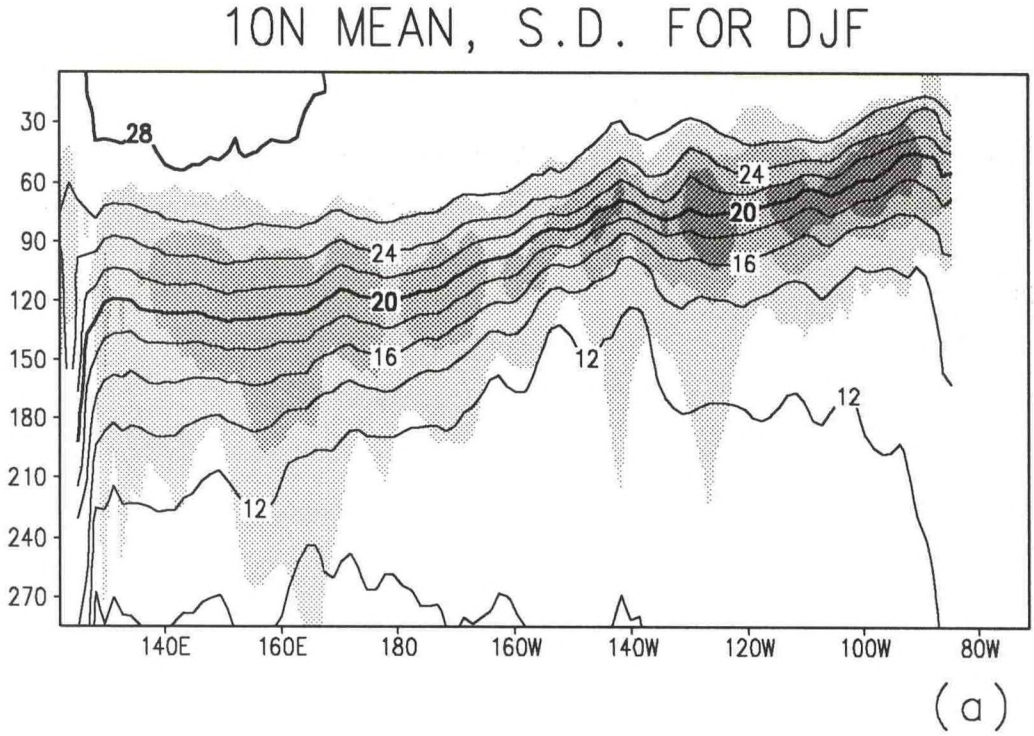

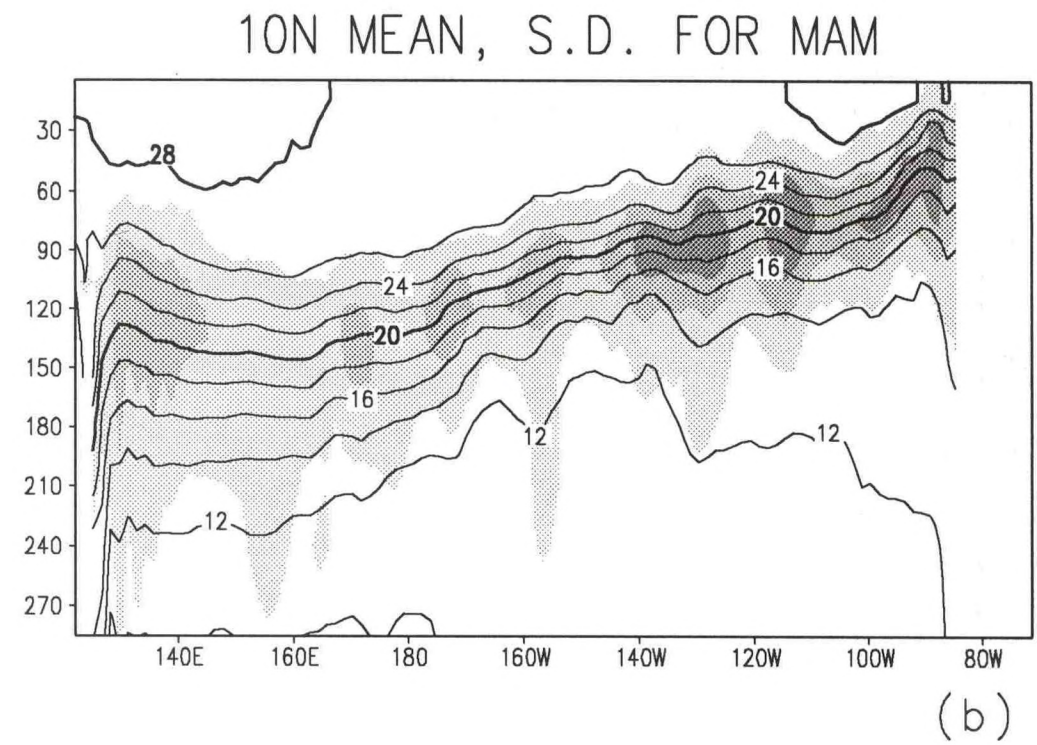

Fig. 12. The longitude-depth section of temperature (°C) at 10°N, seasonal mean and monthly standard deviation using all December-February months in the ten-year record (a). As in (a) except using all March-May months (b). Shading for standard deviations > 1°C (light), 2°C (medium), and 3°C (dark).

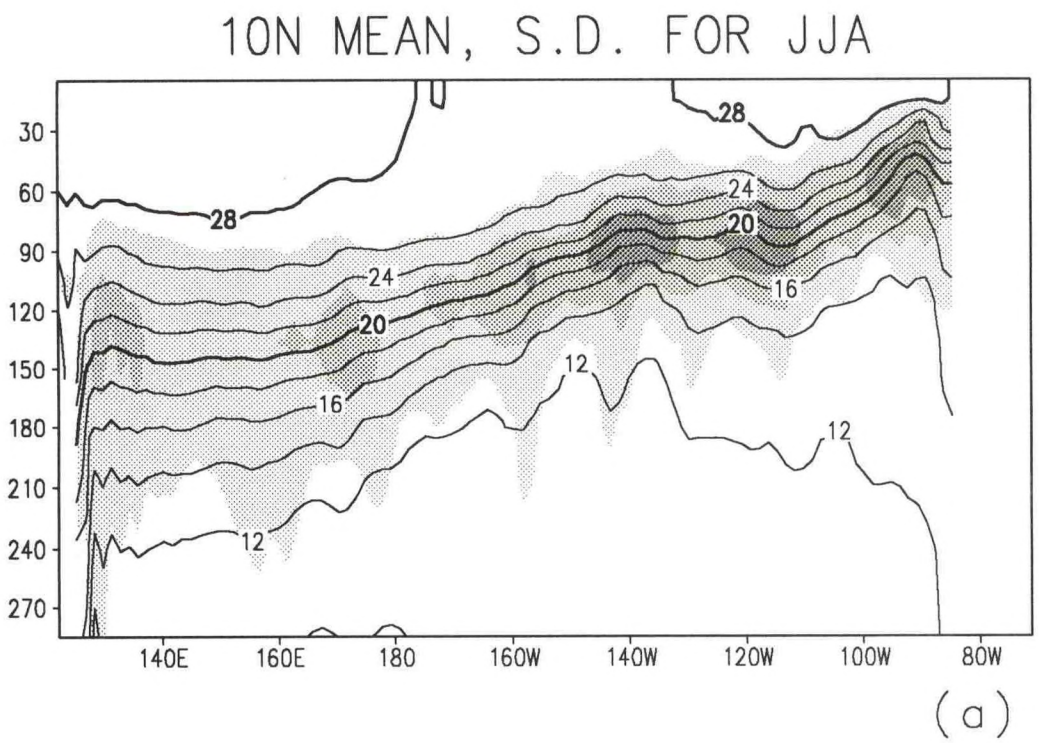

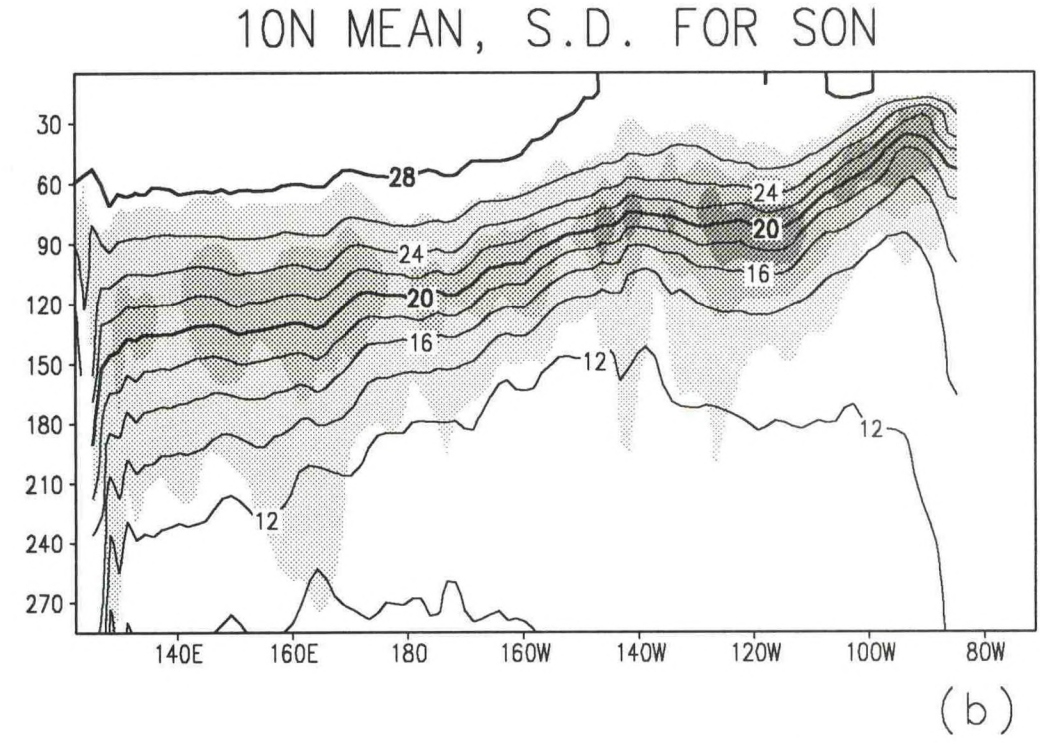

Fig. 13. The longitude-depth section of temperature (°C) at 10°N, seasonal mean and monthly standard deviation using all June-August months in the ten-year record (a). As in (a) except using all September-November months (b). Shading for standard deviations > 1°C (light), 2°C (medium), and 3°C (dark).

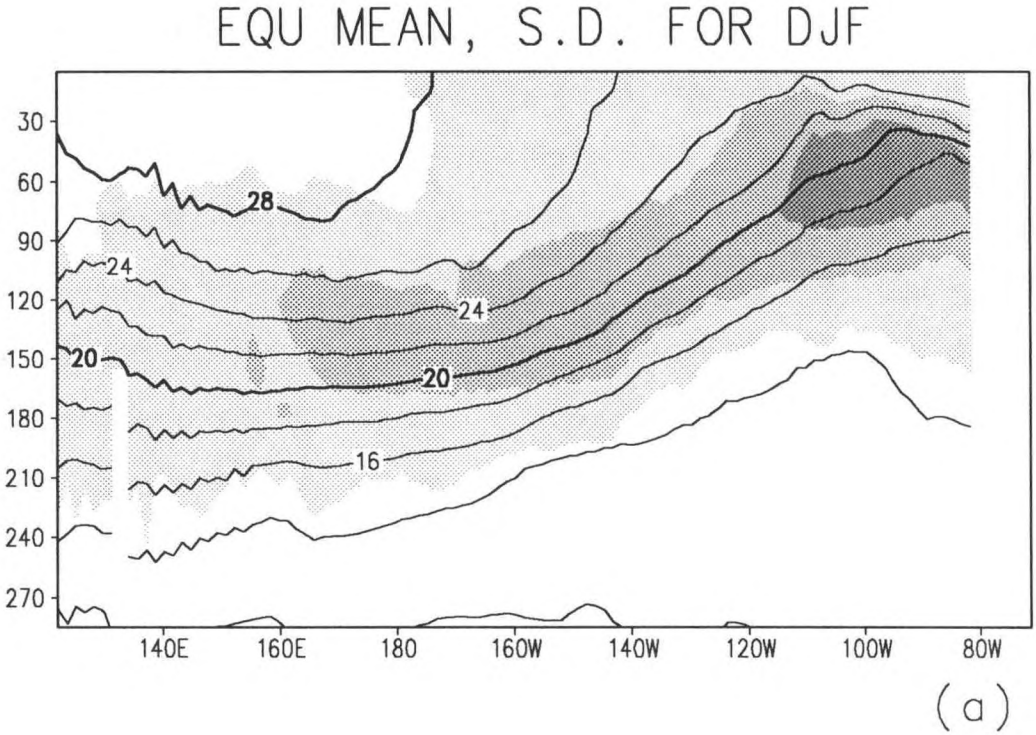

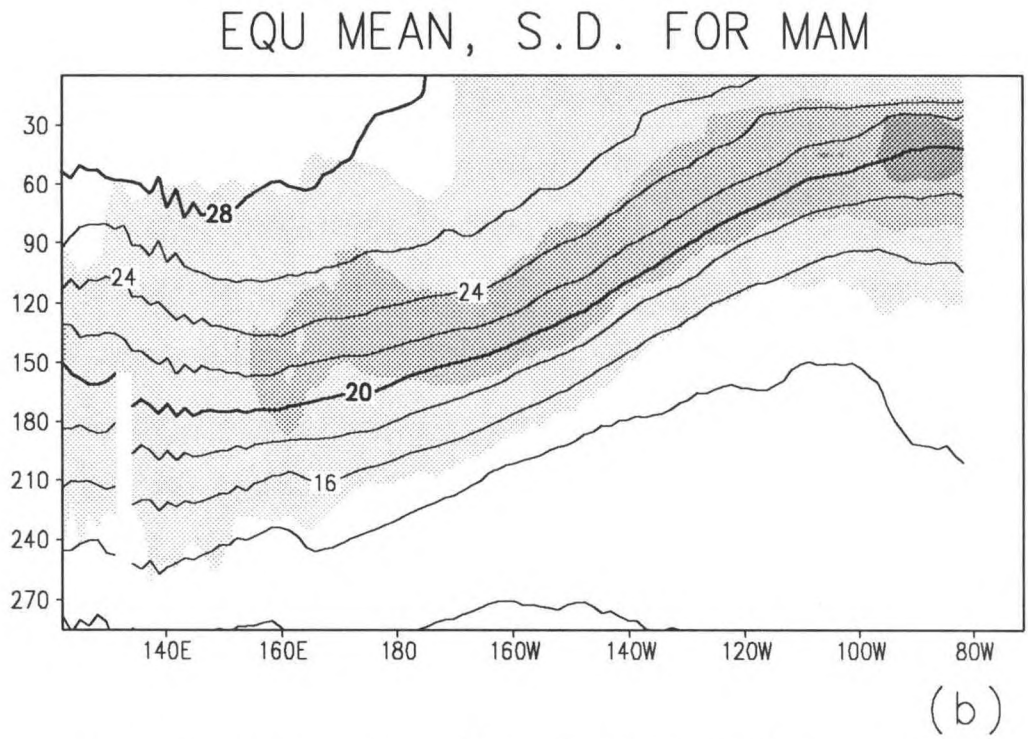

Fig. 14. The longitude-depth section of temperature at the equator (°C), seasonal mean and monthly standard deviation (a) using all December-February months in the ten-year record. As in (a) except using all March-May months (b). Shading for standard deviations > 1°C (light), 2°C (medium), and 3°C (dark).

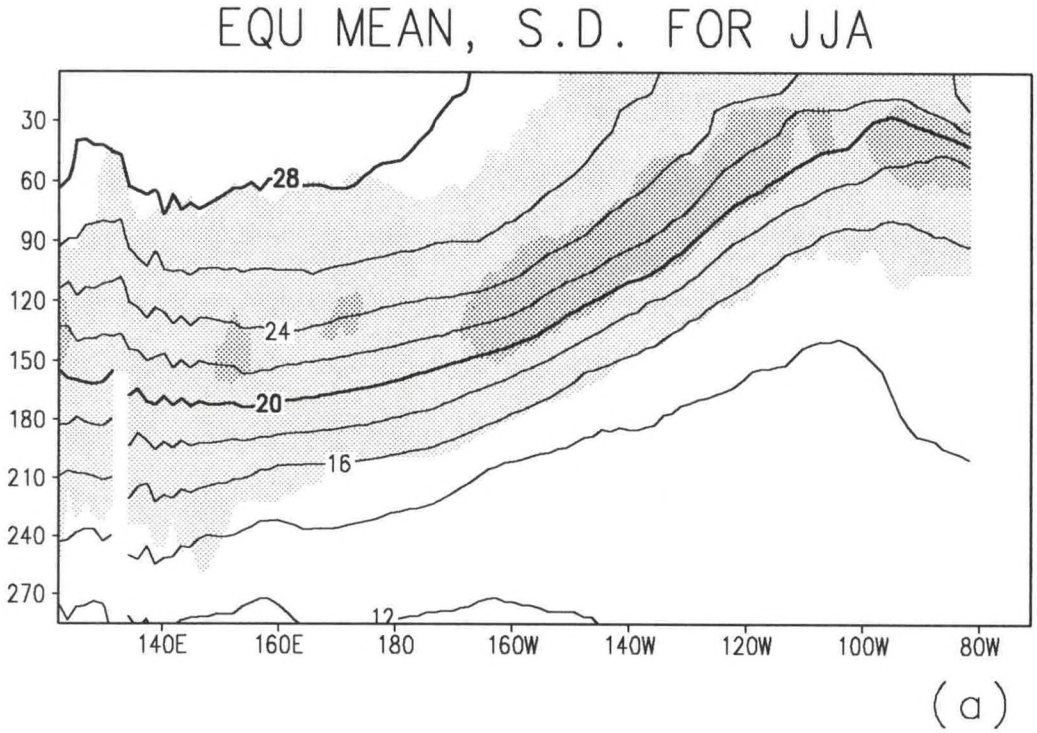

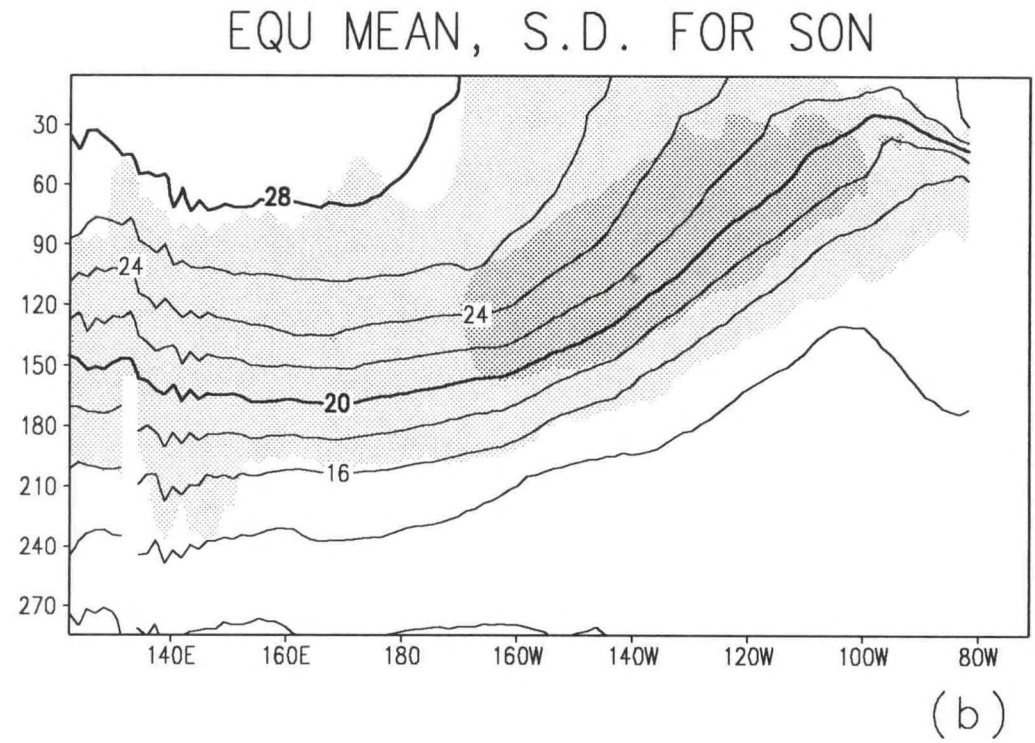

Fig. 15. The longitude-depth section of temperature (°C) at the equator, seasonal mean and monthly standard deviation using all June-August months in the ten-year record (a). As in (a) except using all September-November months (b). Shading for standard deviations > 1°C (light), 2°C (medium), and 3°C (dark).

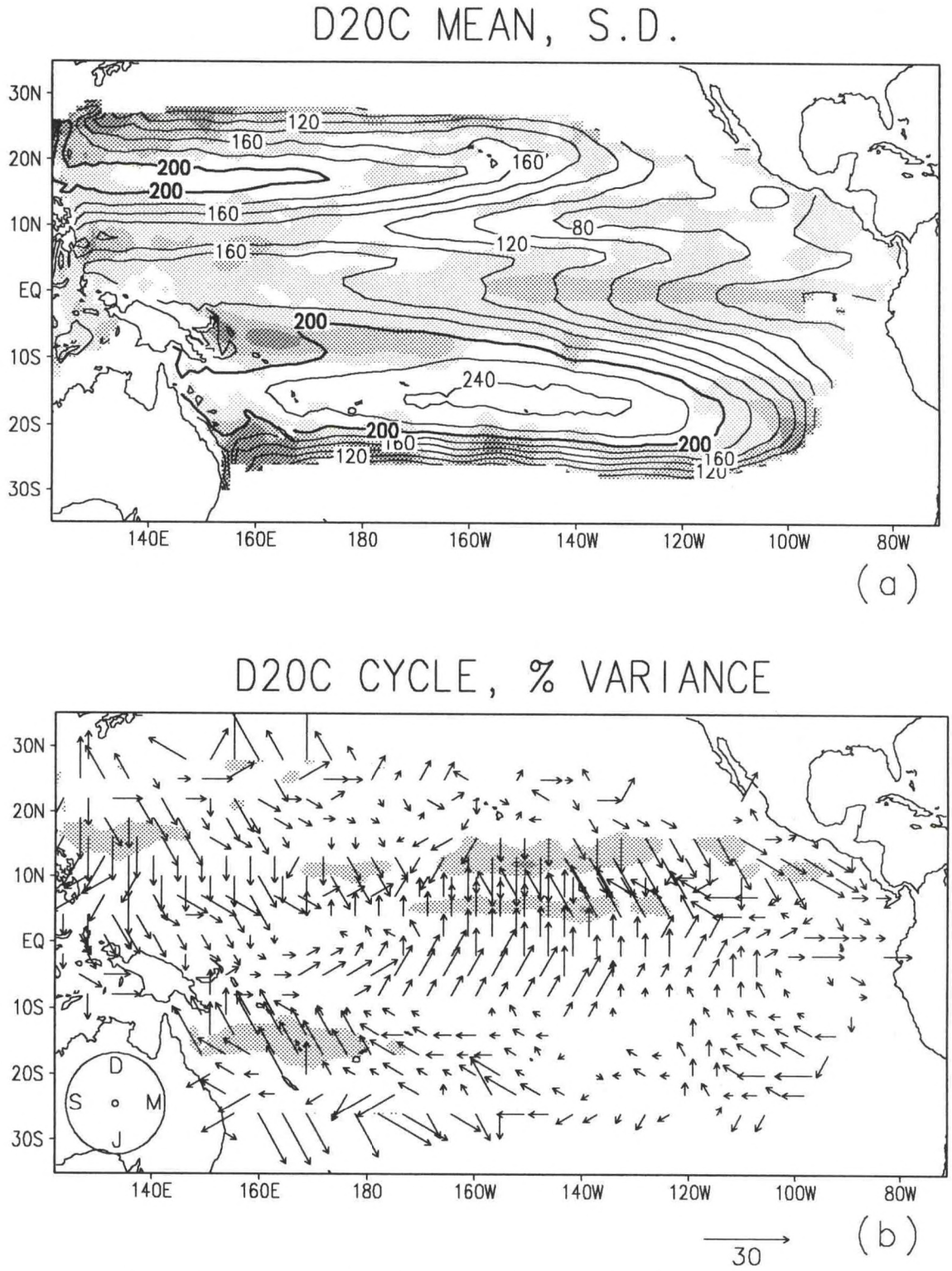

Fig. 16. The depth (m) of the 20°C isotherm ten-year mean and monthly standard deviation (a). Shading for standard deviations > 15 m (light), 20 m (medium), and 25 m (dark). Annual cycle harmonic dials and the percent variance due to the annual cycle (b). Medium shading for > 30% variance accounted, dark shading for > 60%. The reference vector has units of meters, otherwise as in Fig. 2.

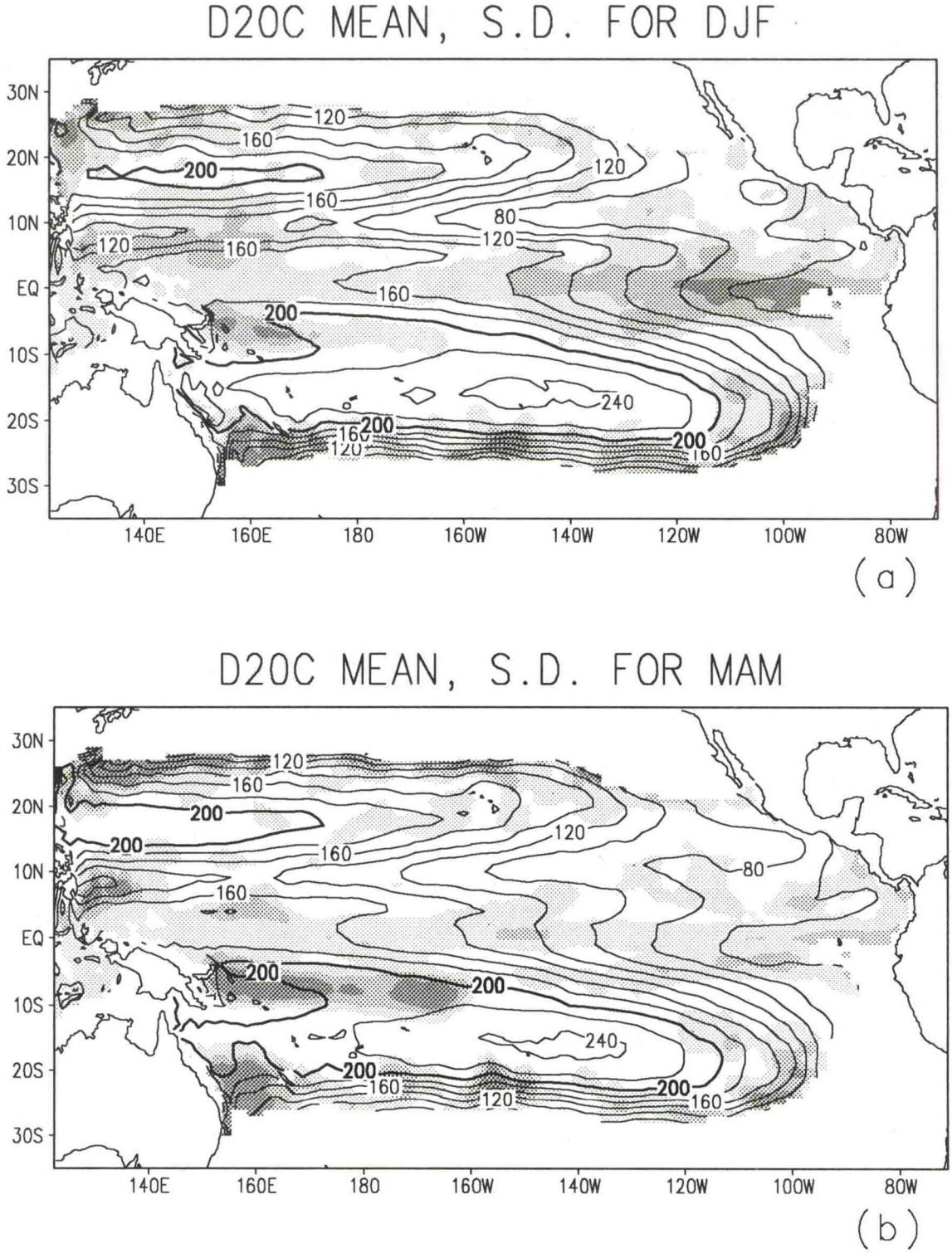

Fig. 17. The depth (m) of the 20°C isotherm, seasonal mean and monthly standard deviation (a) using all December-February months in the ten-year record. As in (a) except using all March-May months (b). Shading for standard deviations > 15 m (light), 20 m (medium), and 25 m (dark).

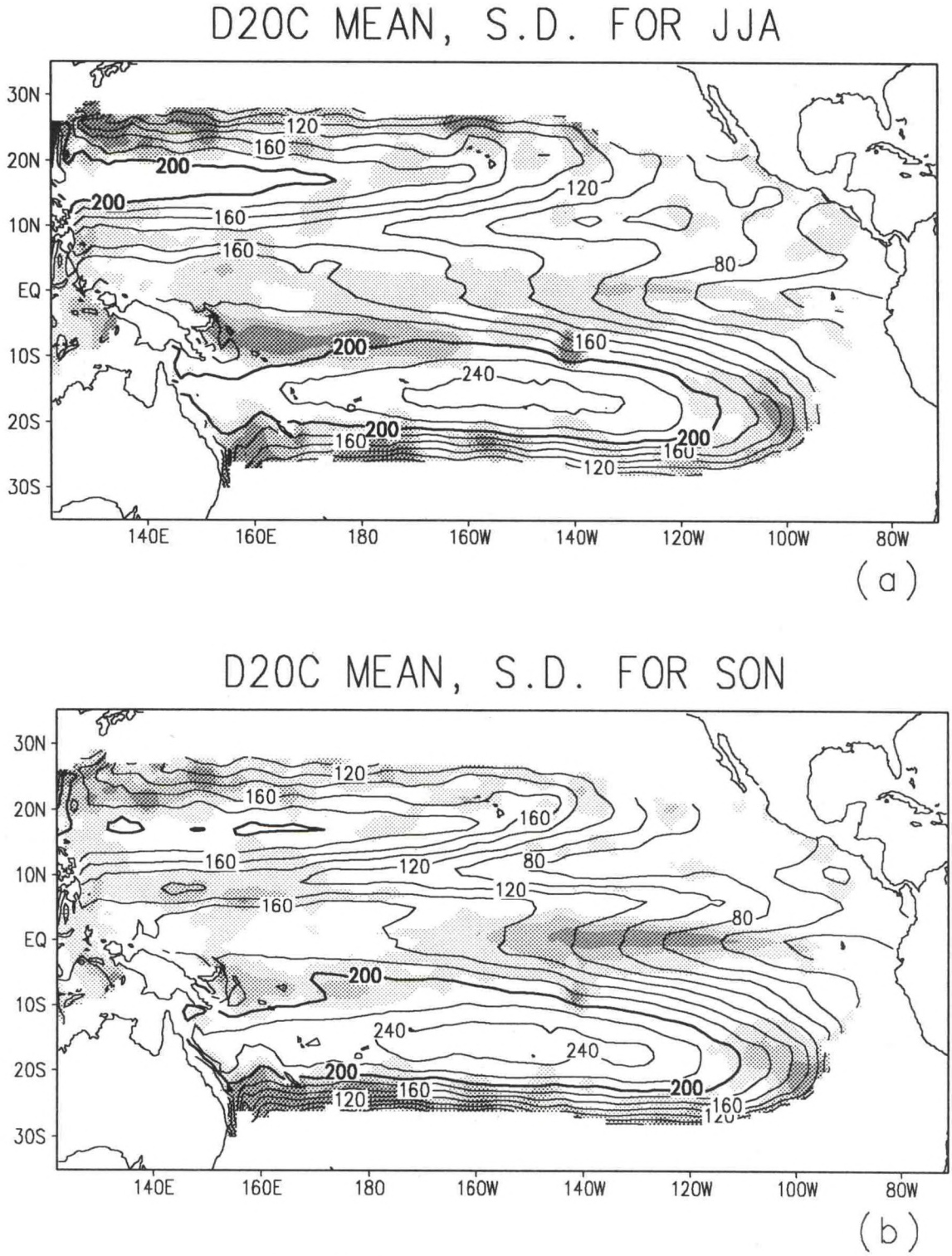

Fig. 18. The depth (m) of the 20°C isotherm seasonal mean and monthly standard deviation using all June-August months in the ten-year record (a). As in (a) except using all September-November months (b). Shading for standard deviations > 15 m (light), 20 m (medium), and 25 m (dark).

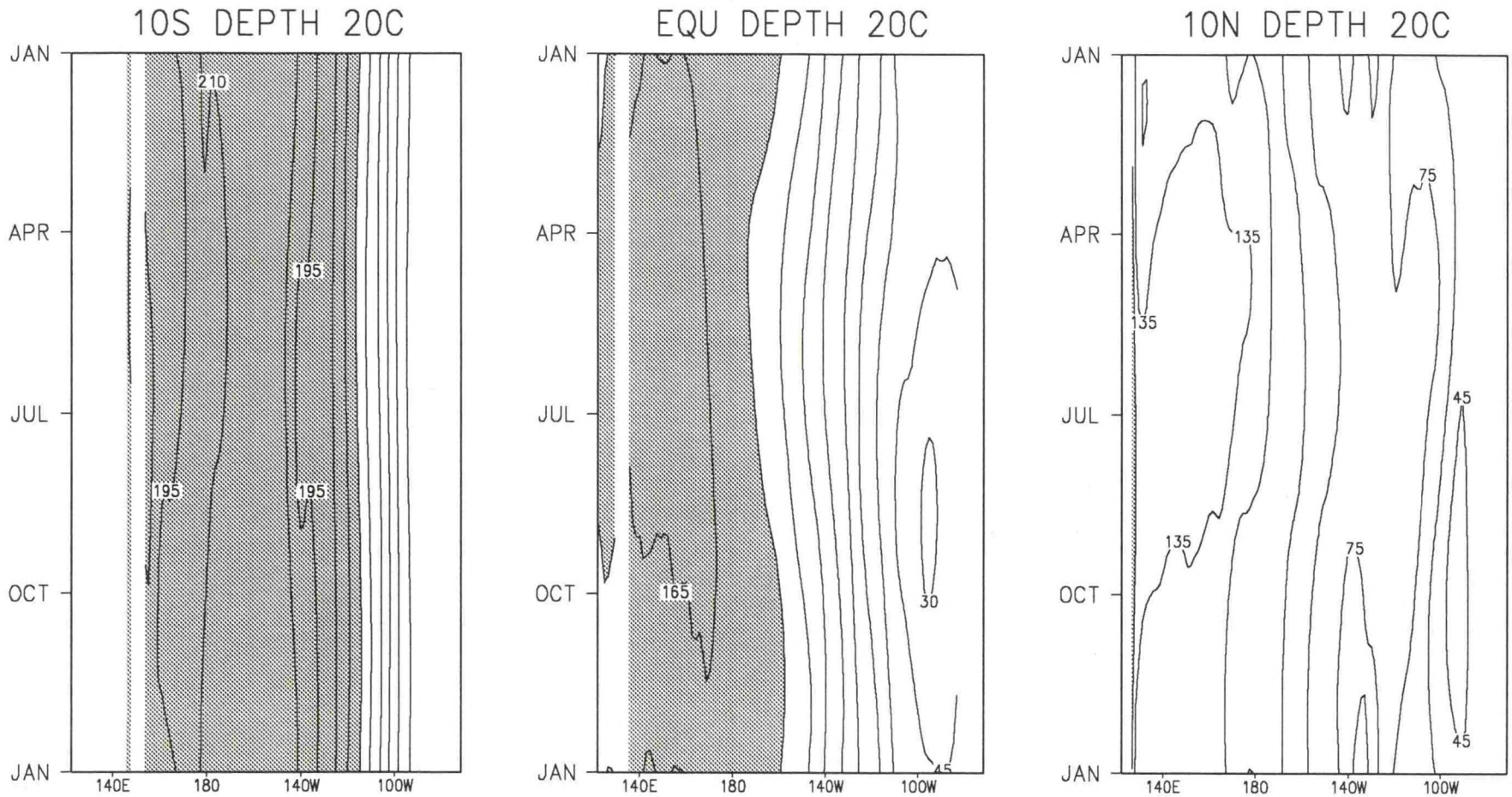

Fig. 19. Time-longitude of the annual cycle of the 20°C isotherm along 10°S, the equator, and 10°N, in meters. Depths greater than 150 m are shaded.

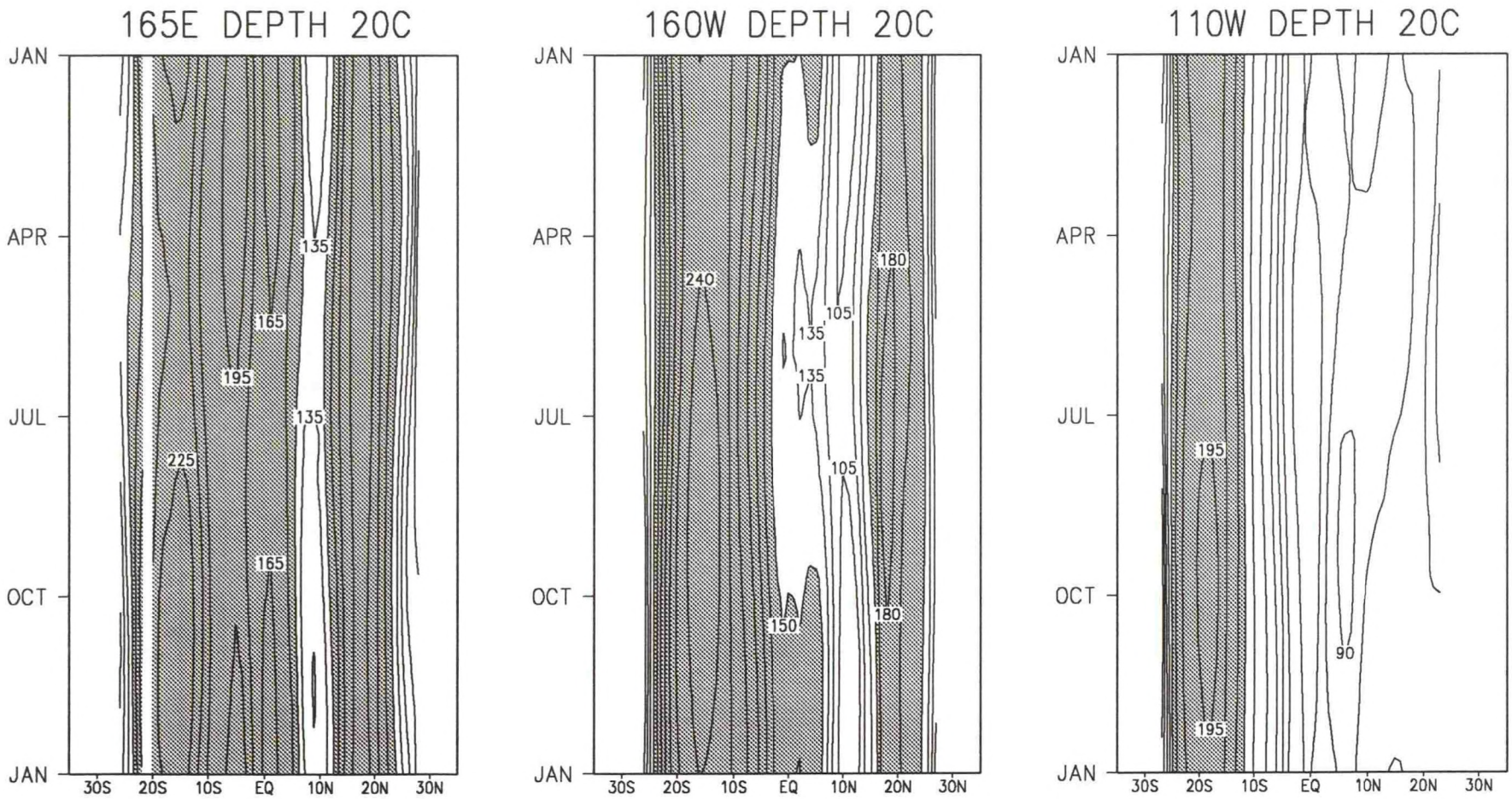

Fig. 20. Time-latitude of the annual cycle of the 20°C isotherm along 165°E, 160°W, and 110°W, in meters. Depths greater than 150 m are shaded.

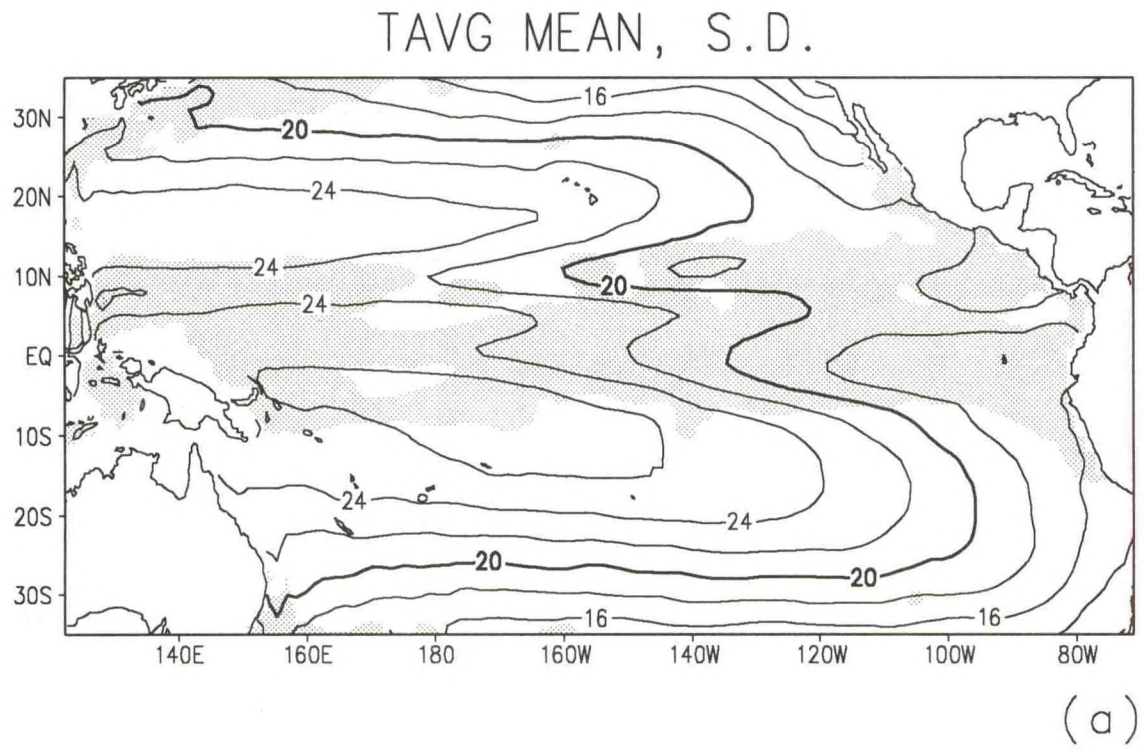

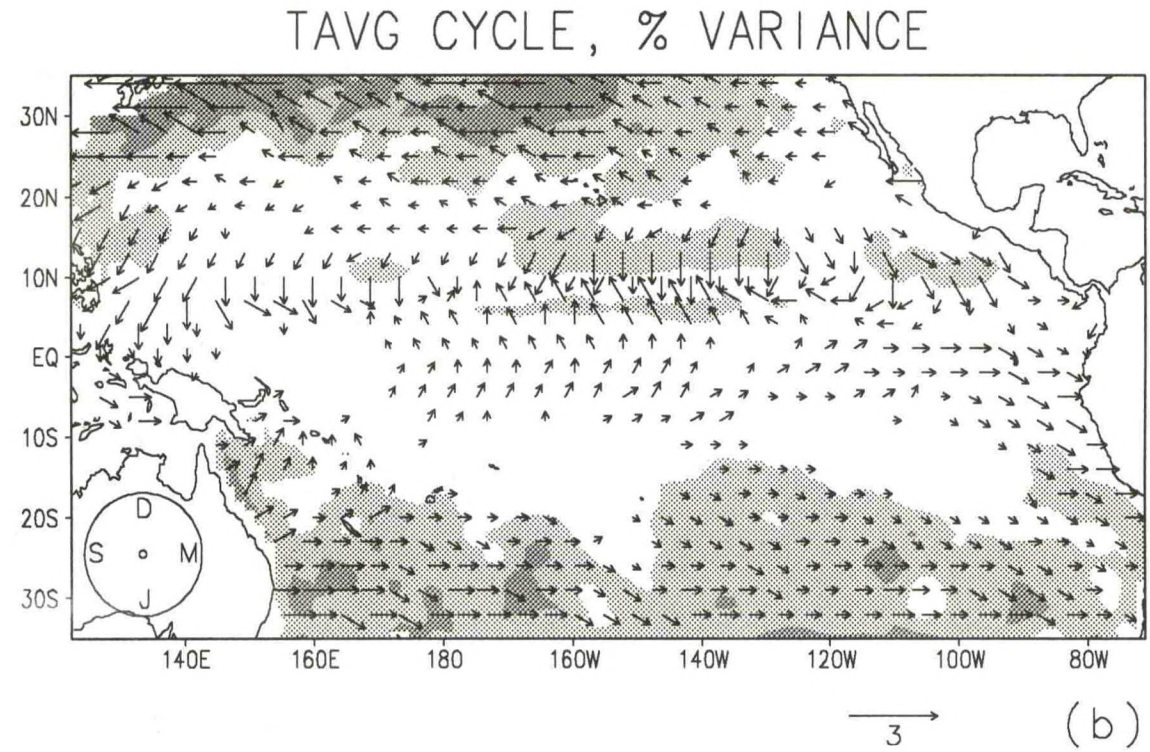

Fig. 21. The average temperature (°C) over the upper 200 m, ten-year mean and monthly standard deviation (a). Shading for standard deviations > 1°C (light), 2°C (medium), and 3°C (dark). Annual cycle harmonic dials and the percent variance due to the annual cycle (b). Medium shading for > 30% variance accounted, dark shading for > 60%. The reference vector has units of °C, otherwise as in Fig. 2.

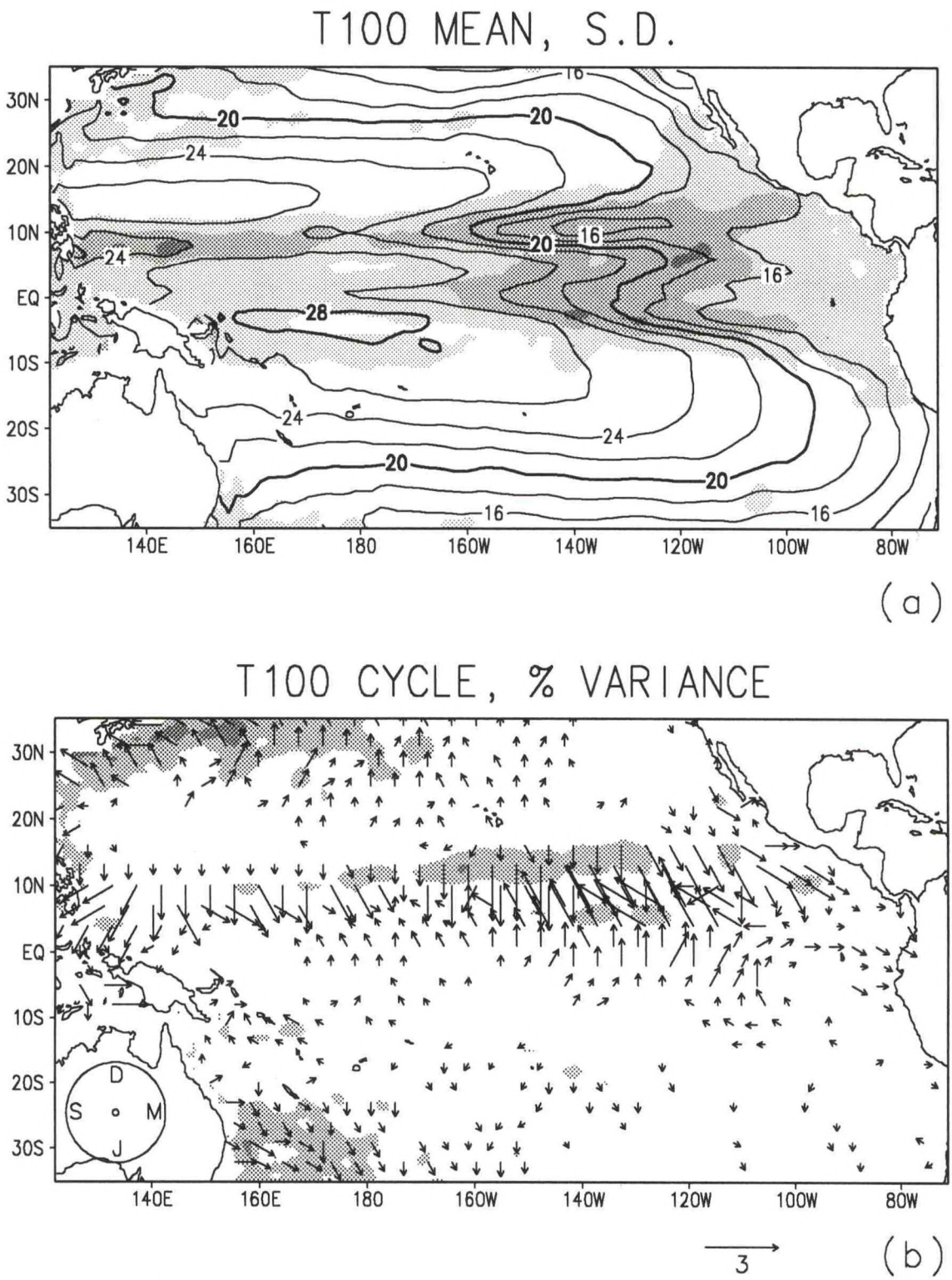

Fig. 22. The temperature (°C) at 100 m, ten-year mean and monthly standard deviation (a). Shading for standard deviations > 1°C (light), 2°C (medium), and 3°C (dark). Annual cycle harmonic dials and the percent variance due to the annual cycle (b). Medium shading for > 30% variance accounted, dark shading for > 60%. The reference vector has units of °C, otherwise as in Fig. 2.

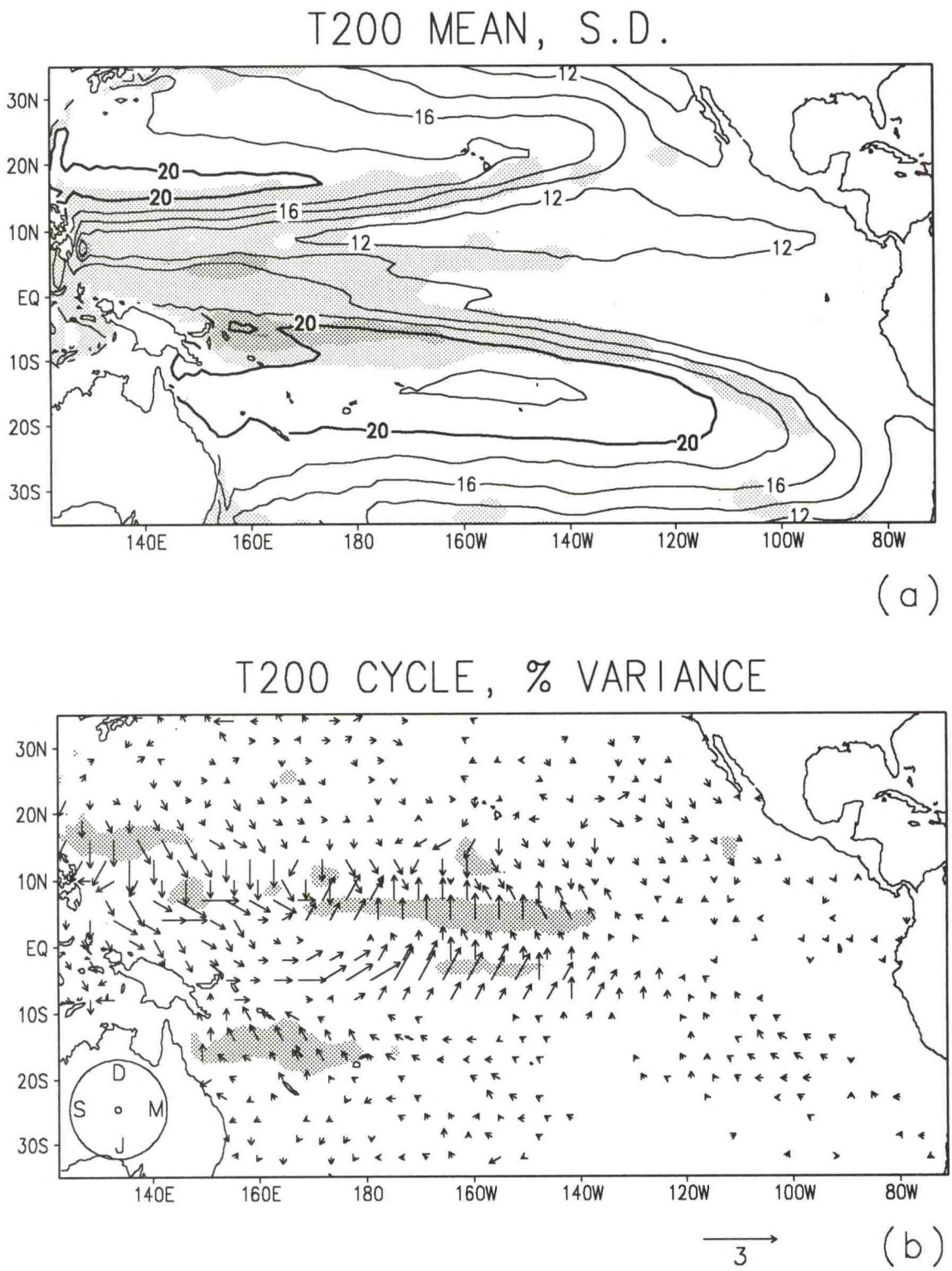

Fig. 23. The temperature (°C) at 200 m, ten-year mean and monthly standard deviation (a). Shading for standard deviations > 1°C (light), 2°C (medium), and 3°C (dark). Annual cycle harmonic dials and the percent variance due to the annual cycle (b). Medium shading for > 30% variance accounted, dark shading for > 60%. The reference vector has units of °C, otherwise as in Fig. 2.

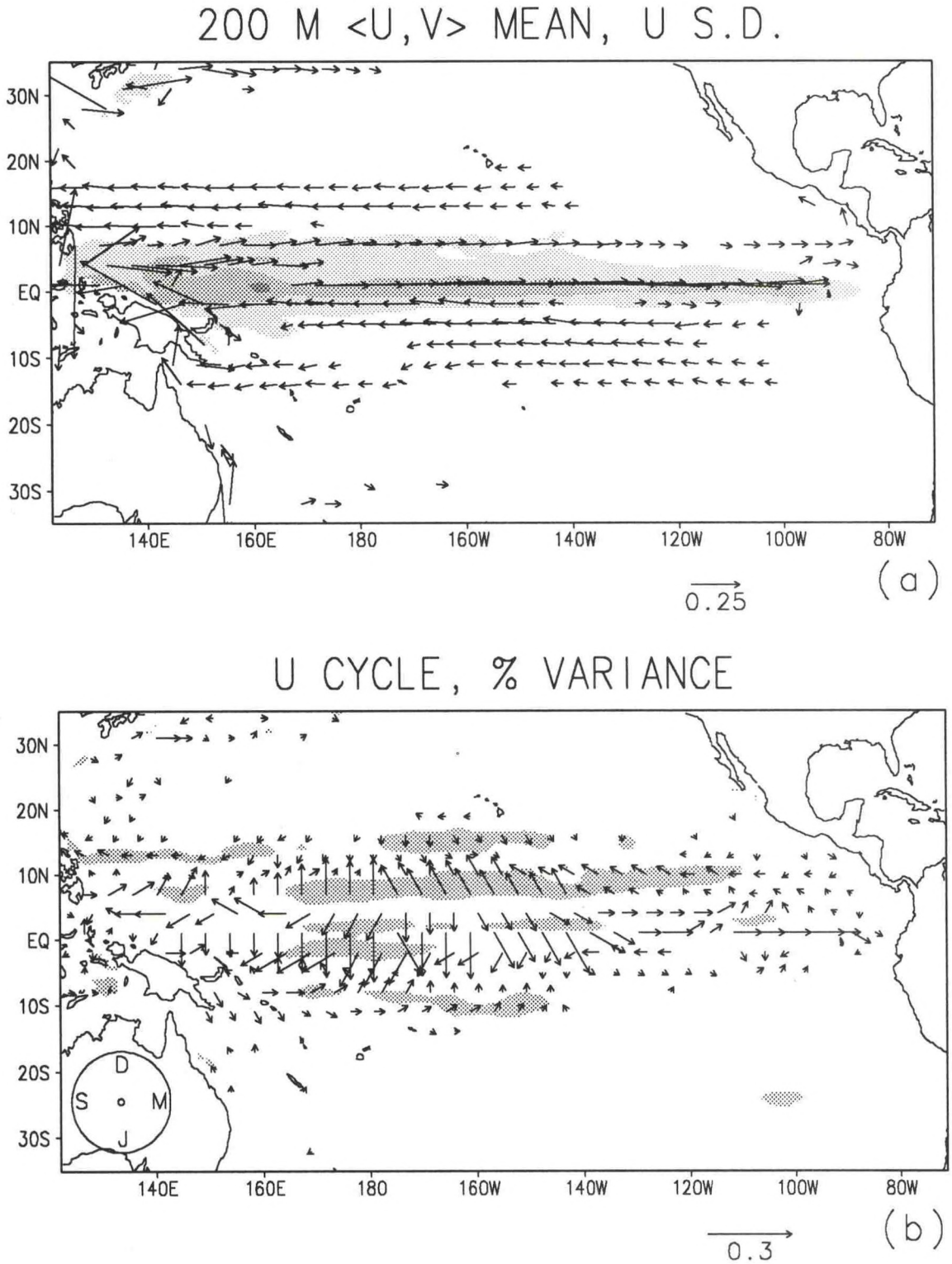

Fig. 24. Horizontal velocity (m s^{-1}) averaged from the surface to 200 meters, ten-year mean and monthly standard deviation. Shading for standard deviations > 0.1 m s^{-1} (light), 0.2 m s^{-1} (medium), and 0.3 m s^{-1} (dark). Zonal velocity annual cycle harmonic dials and percent variance due to the annual cycle (b). Medium shading for > 30% variance accounted, dark shading for > 60%. The reference vector has units of m s^{-1}, otherwise as in Fig. 2.

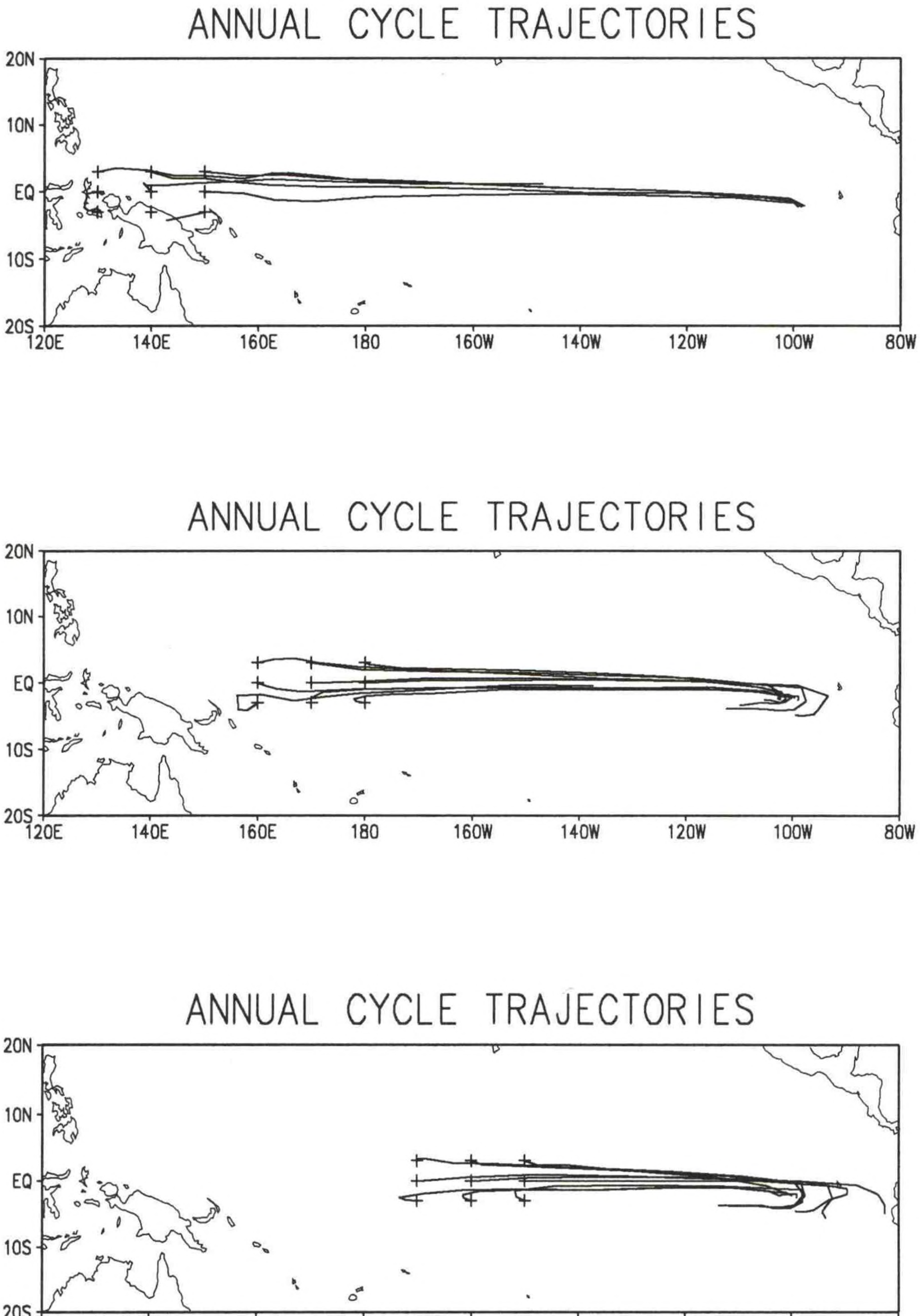

Fig. 25. Trajectories of water flow along the depth of the 20°C isotherm over the annual cycle for parcels starting at 3°S, the equator, and 3°N. Starting locations, for January, are shown by the crosses.

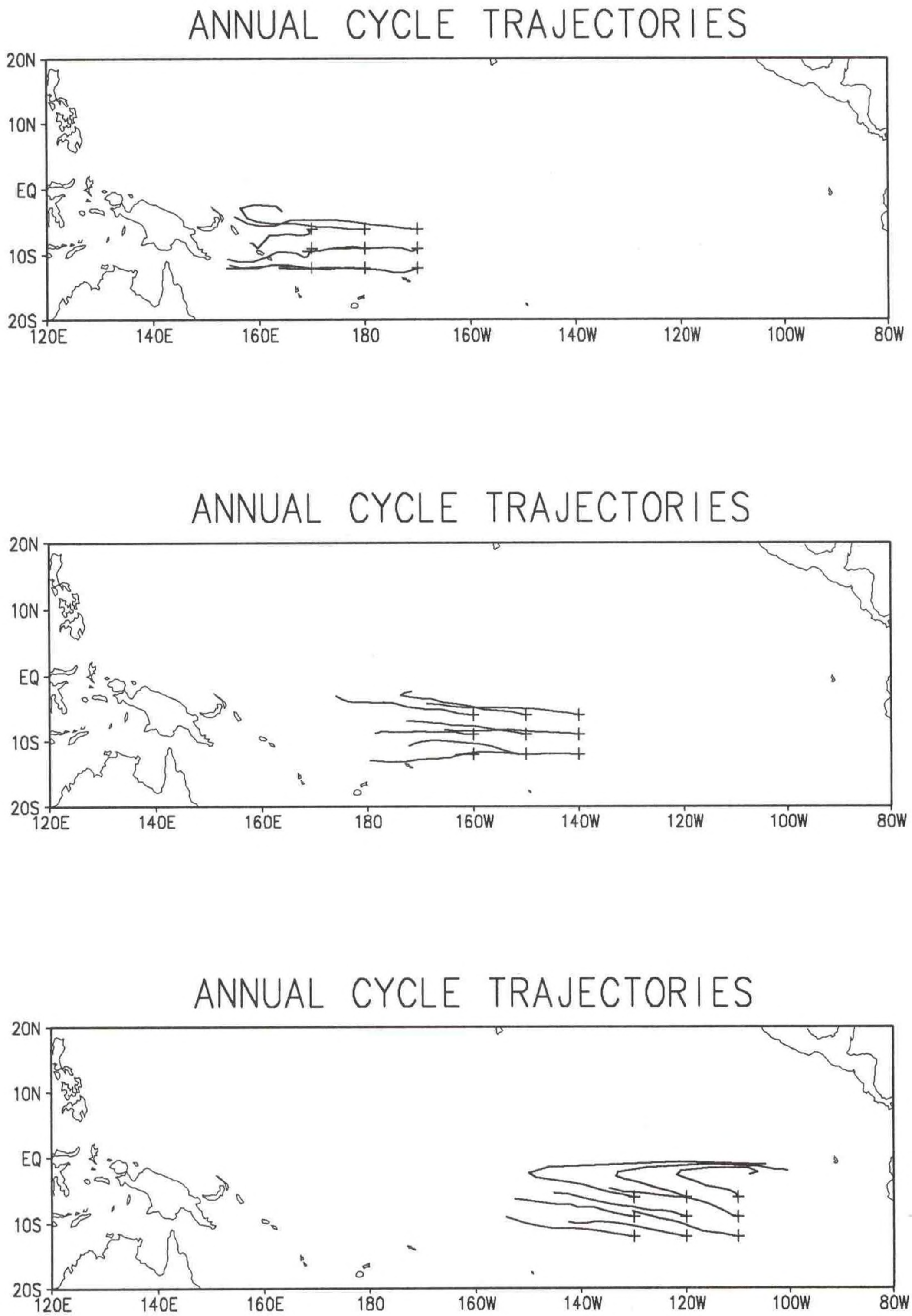

Fig. 26. Trajectories of water flow along the depth of the 20°C isotherm over the annual cycle for parcels starting at 6°S, 9°S, and 12°S. Starting locations, for January, are shown by the crosses.

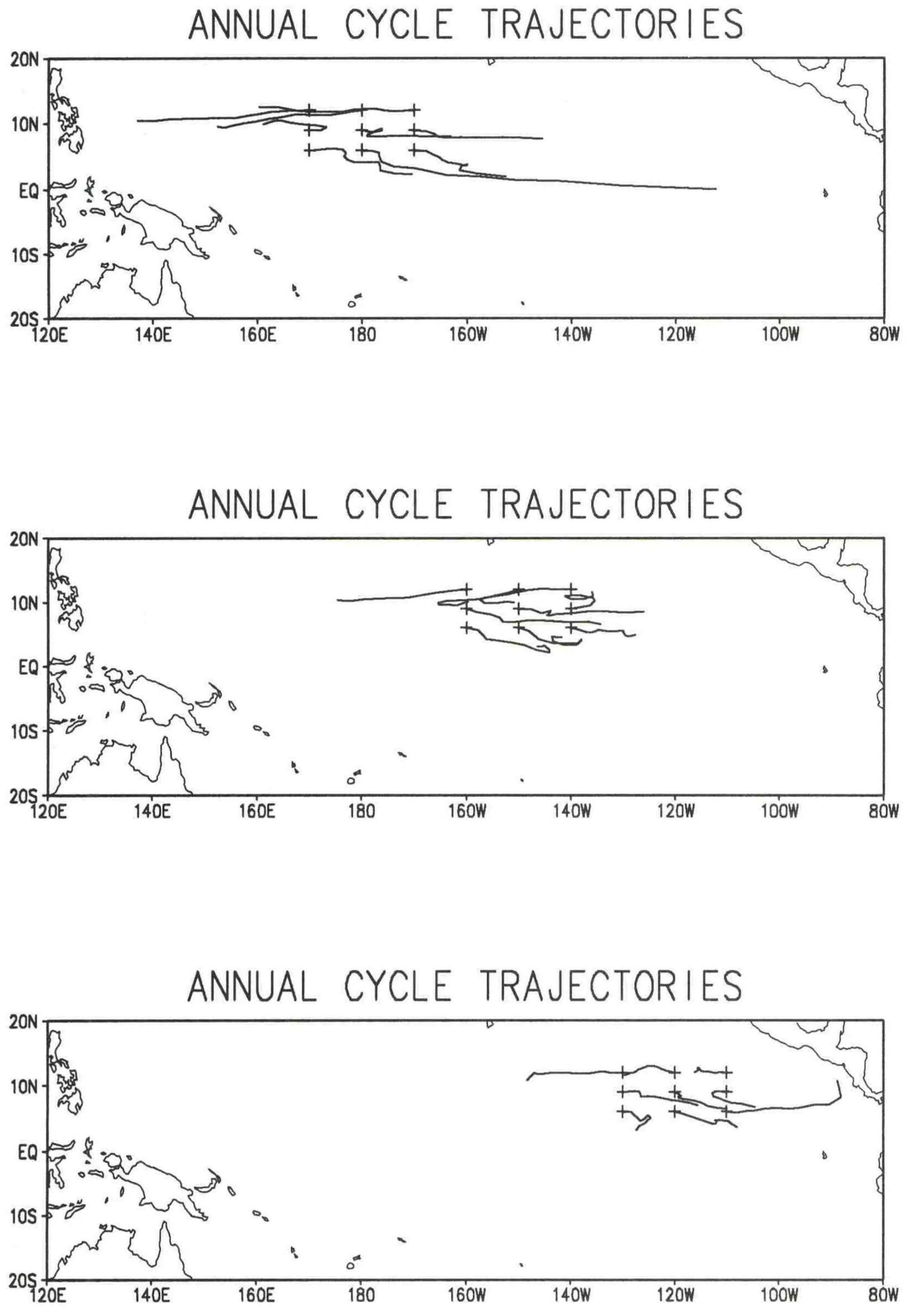

Fig. 27. Trajectories of water flow along the depth of the 20°C isotherm over the annual cycle for parcels starting at 6°N, 9°N, and 12°N. Starting locations, for January, are shown by the crosses.

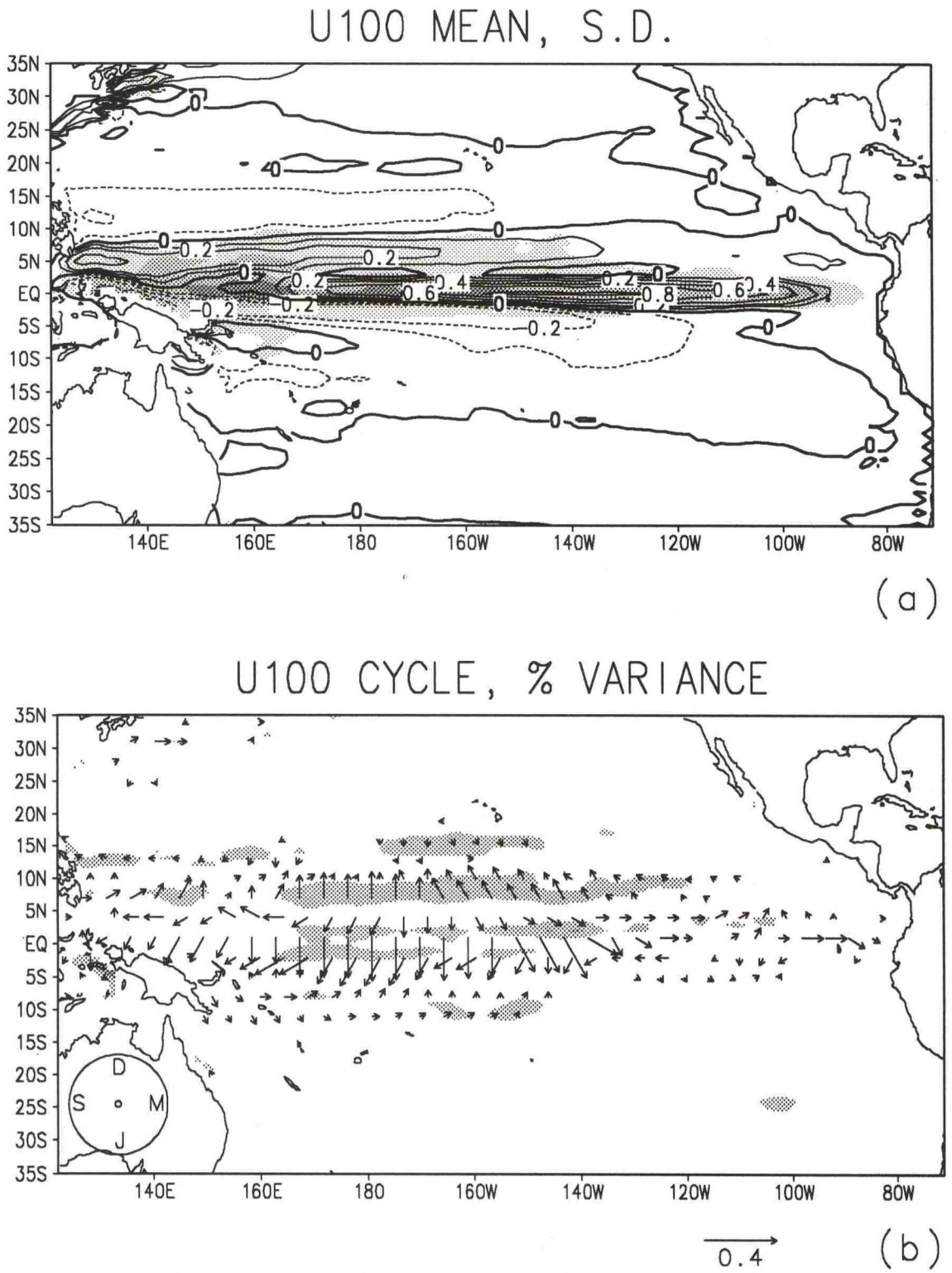

Fig. 28. Ten-year mean and monthly standard deviation of zonal velocity (m s^{-1}) at 100 m (a). Shading for standard deviations > 0.1 m s^{-1} (light), 0.2 m s^{-1} (medium), and 0.3 m s^{-1} (dark). The contour interval is 0.2, except that the ± 0.1 contours are also shown. Zonal velocity annual cycle harmonic dials and percent variance due to the annual cycle (b). Medium shading for > 30% and dark shading for > 60% explained variance. The reference vector has units of m s^{-1}, otherwise as in Fig. 2.

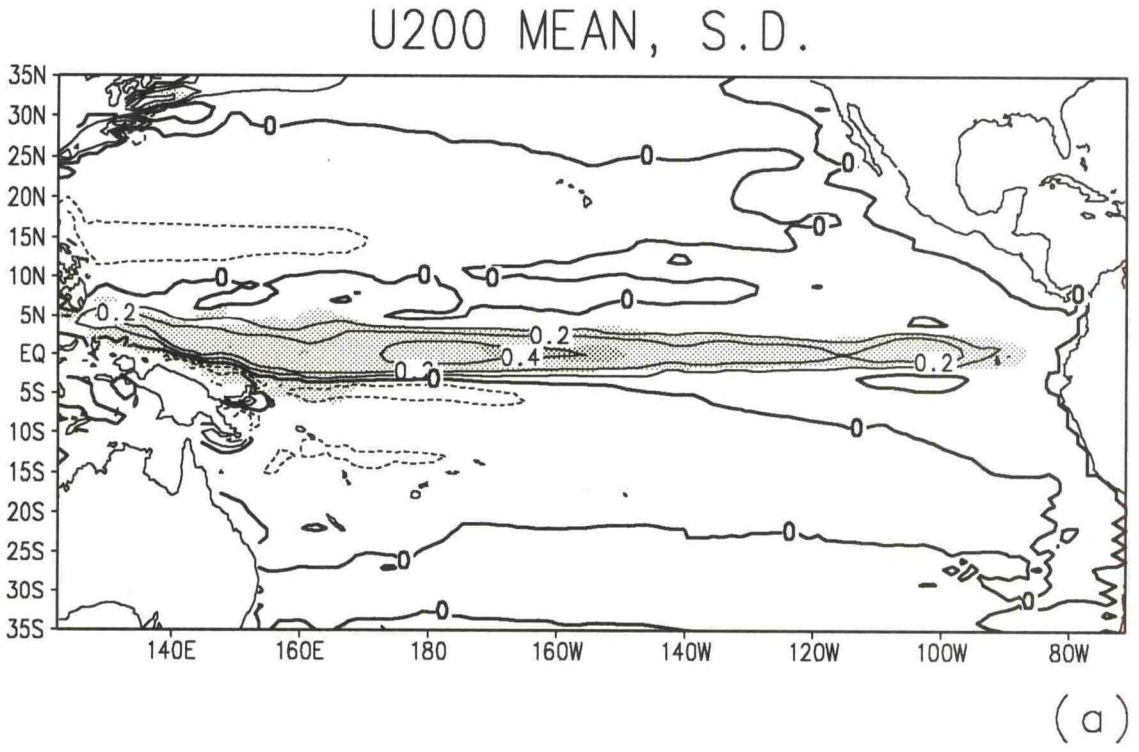

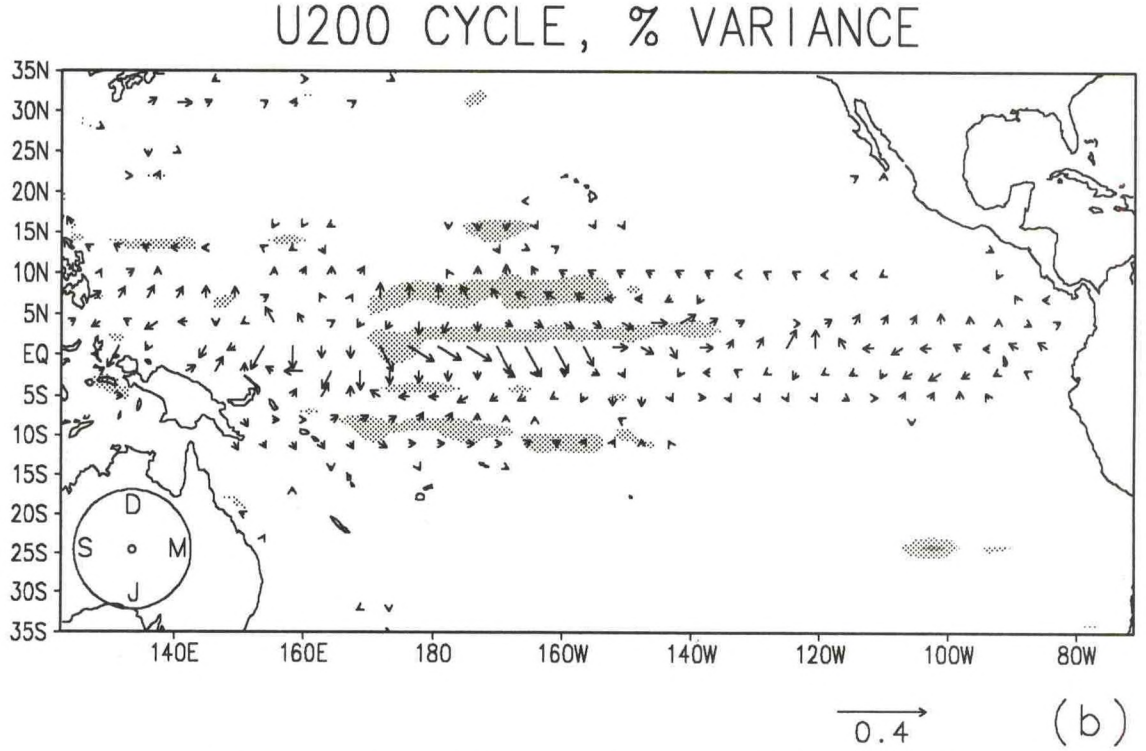

Fig. 29. Ten-year mean and monthly standard deviation of zonal velocity (m s^{-1}) at 200 m (a). Shading for standard deviations > 0.1 m s^{-1} (light), 0.2 m s^{-1} (medium), and 0.3 m s^{-1} (dark). The contour interval is 0.2, except that the ± 0.1 contours are also shown. Zonal velocity annual cycle harmonic dials and percent variance due to the annual cycle (b). Medium shading for > 30% and dark shading for > 60% explained variance. The reference vector has units of m s^{-1}, otherwise as in Fig. 2.

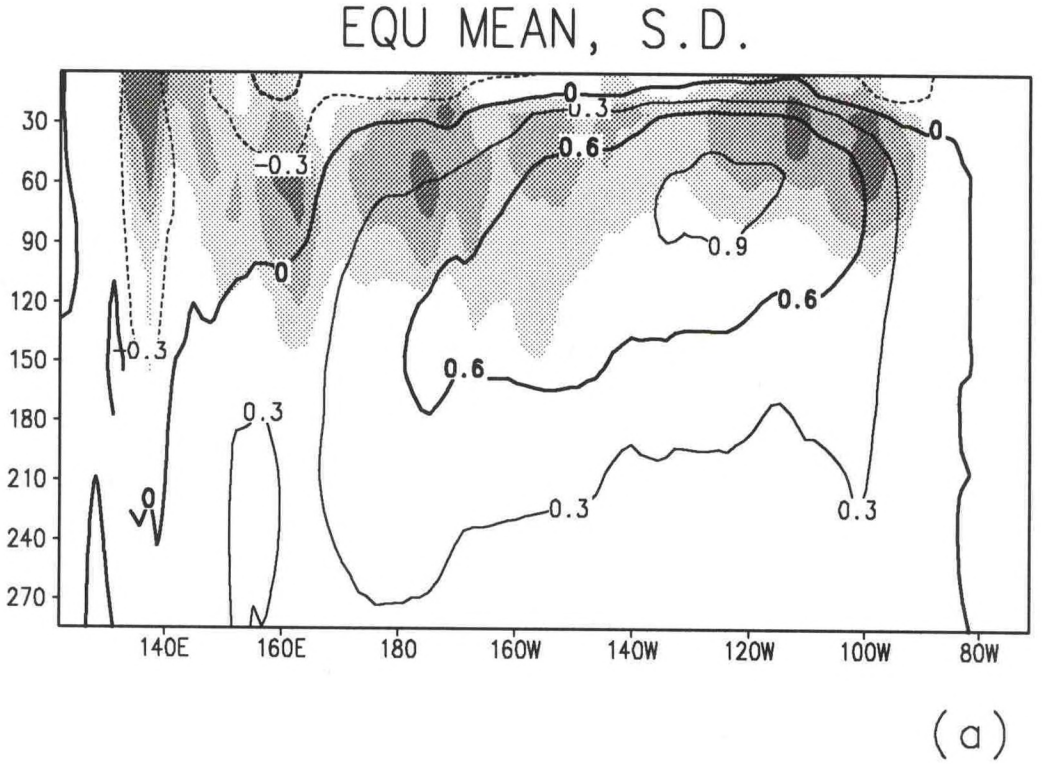

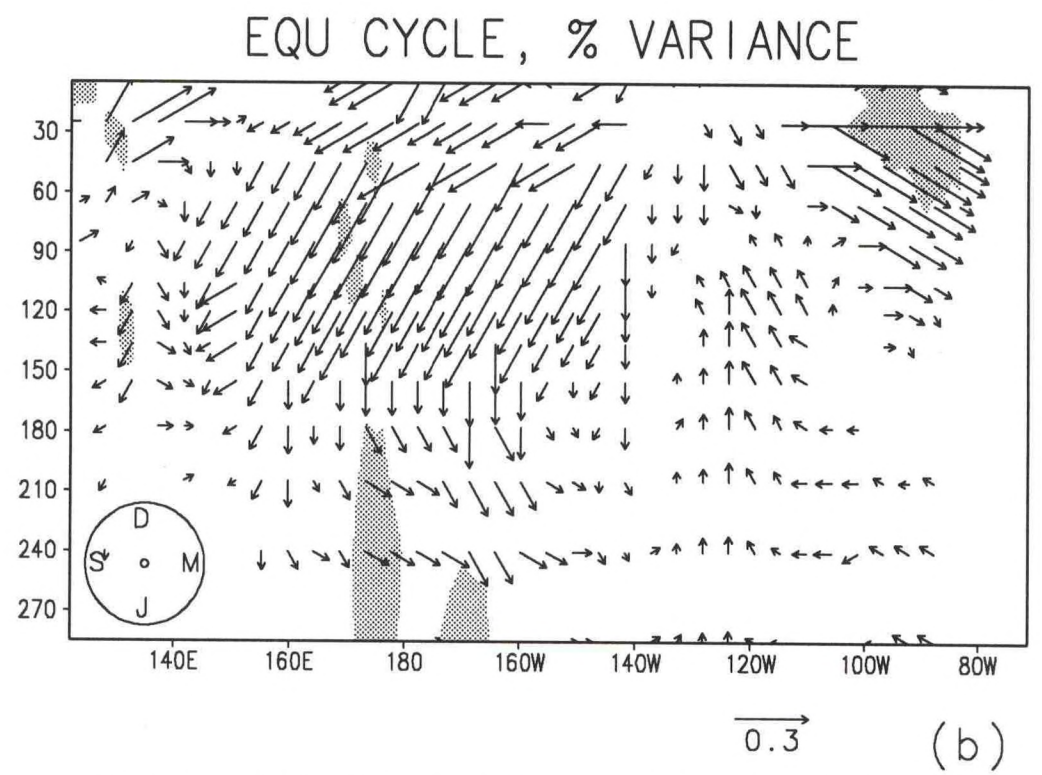

Fig. 30. The longitude-depth section of zonal velocity on the equator (m s^{-1}) ten-year mean and monthly standard deviation (a). Shading for standard deviations > 0.3 m s^{-1} (light), 0.35 m s^{-1} (medium), and 0.4 m s^{-1} (dark). Zonal velocity annual cycle harmonic dials and percent variance due to the annual cycle (b). Medium shading for > 30% and dark shading for > 60% explained variance. The reference vector has units of m s^{-1}, otherwise as in Fig. 2.

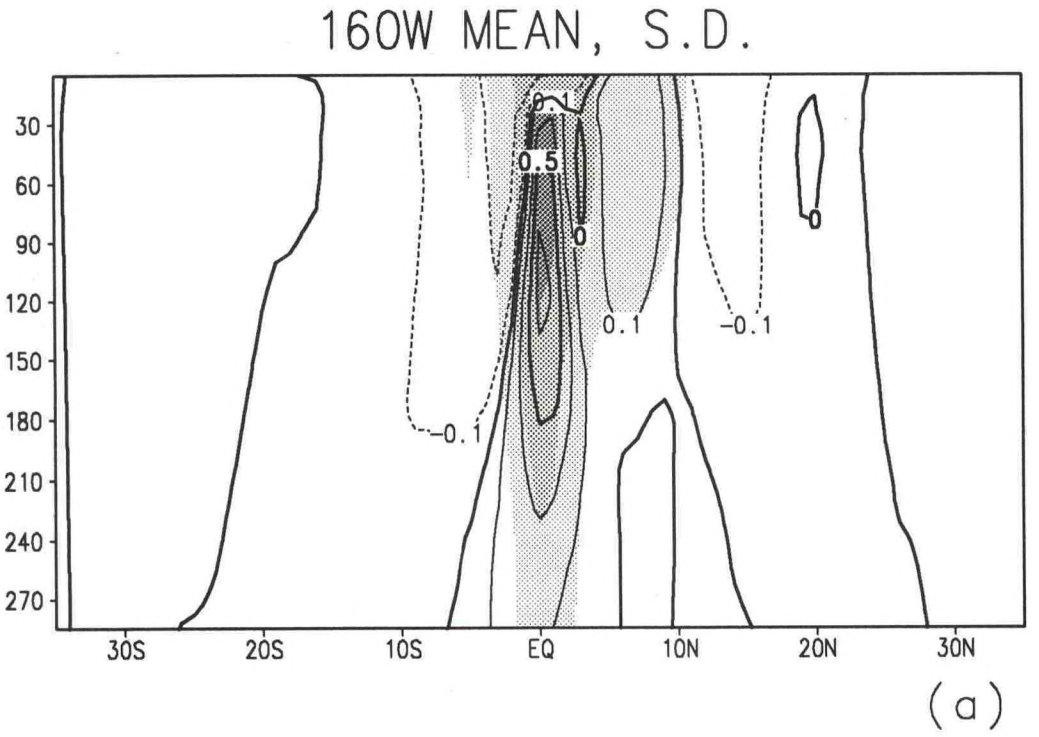

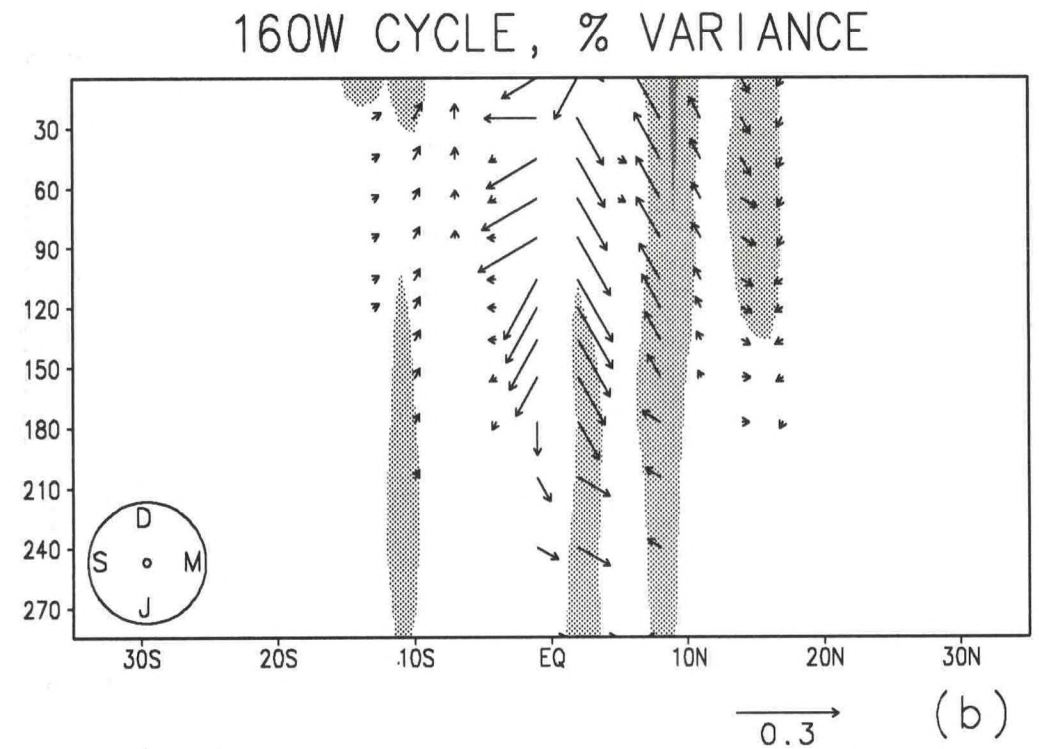

Fig. 31. The zonal velocity (m s^{-1}) at 160°W ten-year mean and monthly standard deviation (a). Shading for standard deviations > 0.1 m s^{-1} (light), 0.2 m s^{-1} (medium), and 0.3 m s^{-1} (dark). Zonal velocity annual cycle harmonic dials and percent variance due to the annual cycle (b). Medium shading for > 30% and dark shading for > 60% explained variance. The reference vector has units of m s^{-1}, otherwise as in Fig. 2.

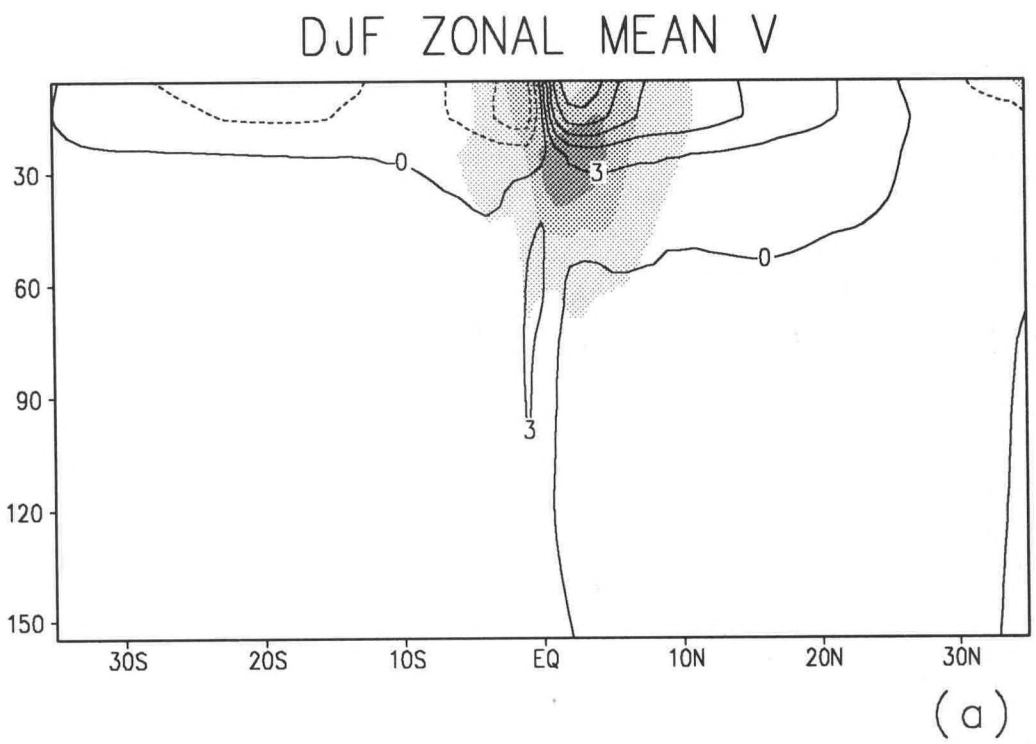

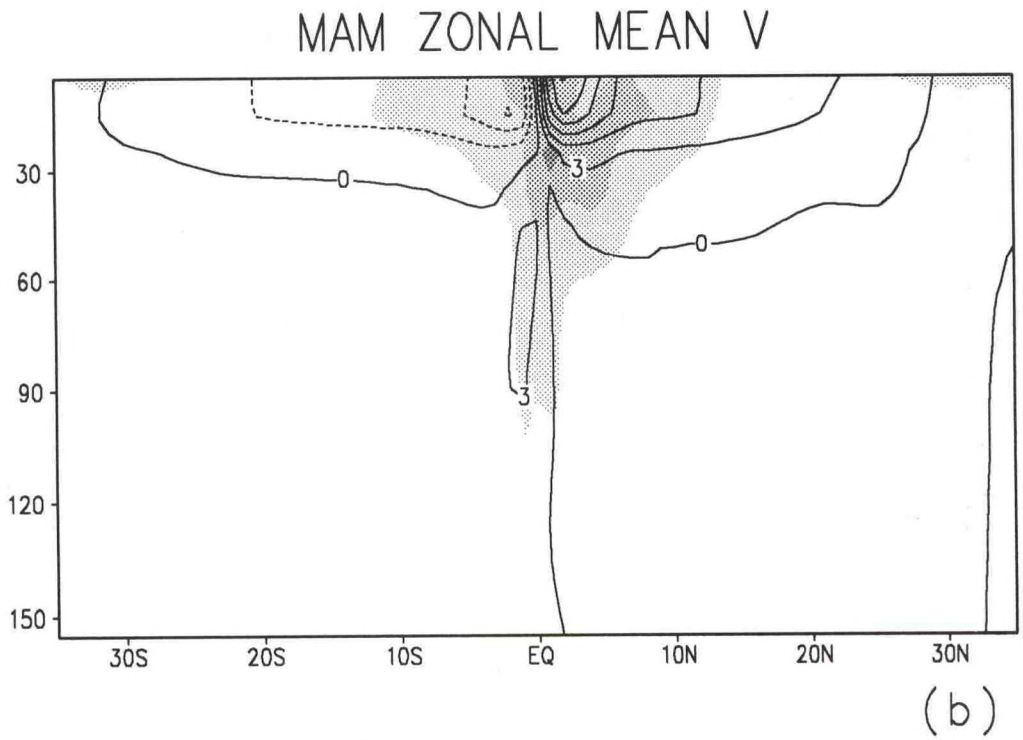

Fig. 32. The zonal average of meridional velocity (10^{-2} m s^{-1}) seasonal mean and monthly standard deviation using all December-February months in the ten-year record (a). As in (a) except using all March-May months (b). Shading for standard deviations > 1 10^{-2} m s^{-1} (light), 2 10^{-2} m s^{-1} (medium), and 3 10^{-2} m s^{-1} (dark).

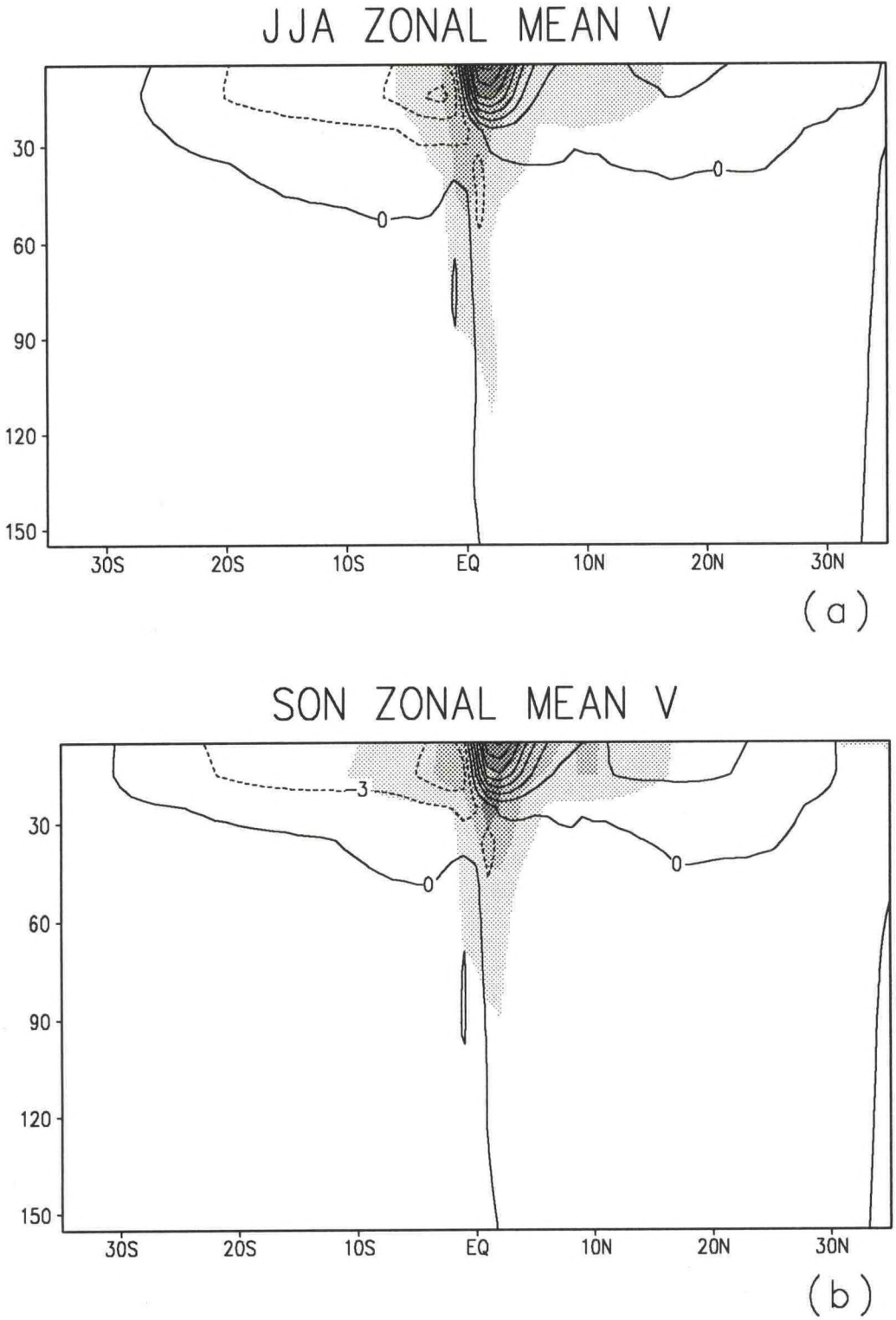

Fig. 33. The zonal average of meridional velocity (10^{-2} m s^{-1}) seasonal mean and monthly standard deviation using all June-August months in the ten-year record (a). As in (a) except using all September-November months (b). Shading for standard deviations > $1x10^{-2}$ m s^{-1} (light), $2x10^{-2}$ m s^{-1} (medium), and $3x10^{-2}$ m s^{-1} (dark).

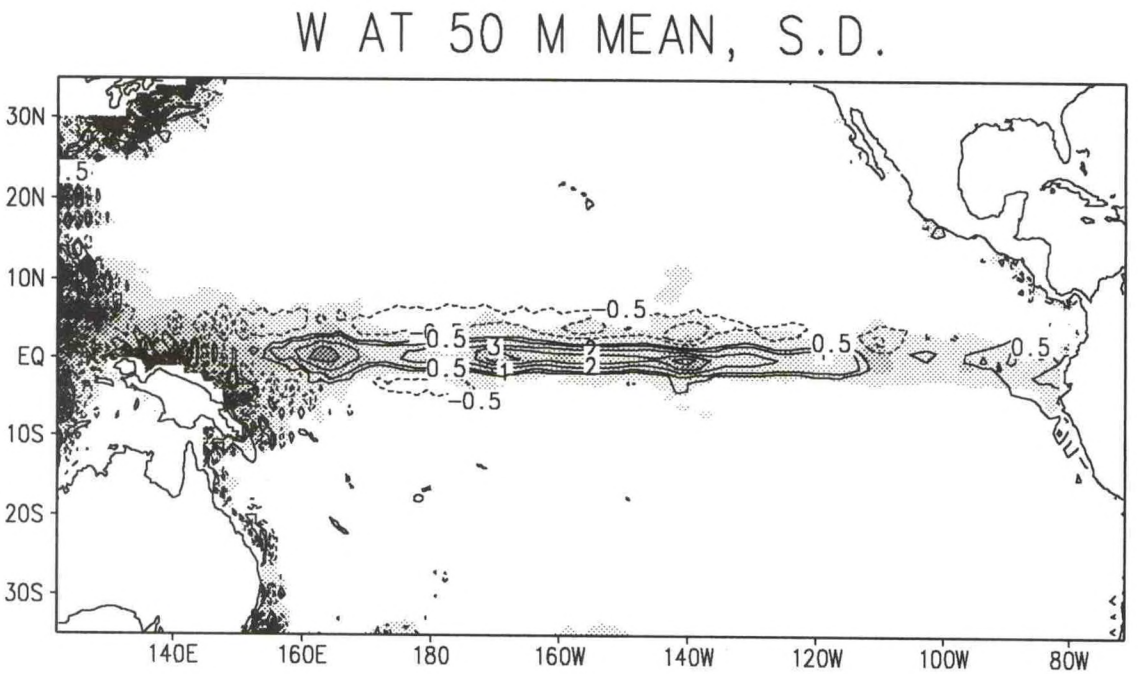

Fig. 34. Vertical velocity at 50 m depth (10^{-5} m s^{-1}) ten-year mean and monthly standard deviation. The contour interval is $1x10^{-5}$ m s^{-1}, except that the $\pm$ $0.5x10^{-5}$ m s^{-1} contour is also shown and the zero contour is omitted. Shading for standard deviations > $1x10^{-5}$ m s^{-1} (light), $2x10^{-5}$ m s^{-1} (medium), and $3x10^{-5}$ m s^{-1} (dark).